

## Article

# Calibration and Validation of Flow Parameters of Irregular Gravel Particles Based on the Multi-Response Concept

Aibin Zhang <sup>1,2</sup>, Zhaohui Wang <sup>1,2,\*</sup> , Quanjie Gao <sup>1,2</sup>, Yiwei Fan <sup>1,2</sup> and Hongxia Wang <sup>3</sup>

<sup>1</sup> Key Laboratory of Metallurgical Equipment and Control Technology of Ministry of Education, Wuhan University of Science and Technology, Wuhan 430081, China

<sup>2</sup> Hubei Key Laboratory of Mechanical Transmission and Manufacturing Engineering, Wuhan University of Science and Technology, Wuhan 430081, China

<sup>3</sup> College of Mechanical Engineering, Hubei University of Automotive Technology, Shiyan 442002, China

\* Correspondence: zhwang@wust.edu.cn

**Abstract:** The discrete element method (DEM) often uses the angle of repose to study the microscopic parameters of particles. This paper proposes a multi-objective optimization method combining realistic modeling of particles and image analysis to calibrate gravel parameters, after obtaining the actual static angle of repose ( $\alpha_{A0R\_S}$ ) and dynamic angle of repose ( $\beta_{A0R\_D}$ ) of the particles by physical tests. The design variables were obtained by Latin hypercube sampling (LHS), and the radial basis function (RBF) surrogate model was used to establish the relationship between the objective function and the design variables. The optimized design of the non-dominated sorting genetic algorithm II (NSGA-II) with the actual angle of repose measurements was used to optimize the design to obtain the best combination of parameters. Finally, the parameter set was validated by a hollow cylinder test, and the relative error between the validation test and the optimized simulation results was only 3.26%. The validation result indicates that the method can be reliably applied to the calibration process of the flow parameters of irregular gravel particles. The development of solid–liquid two-phase flow and the wear behavior of centrifugal pumps were investigated using the parameter set. The results show that the increase in cumulative tangential contact forces inside the volute of centrifugal pumps makes it the component most likely to develop wear behavior. The results also illustrate the significant meaning of the accurate application of the discrete element method for improving the efficient production of industrial scenarios.



**Citation:** Zhang, A.; Wang, Z.; Gao, Q.; Fan, Y.; Wang, H. Calibration and Validation of Flow Parameters of Irregular Gravel Particles Based on the Multi-Response Concept.

*Processes* **2023**, *11*, 268. <https://doi.org/10.3390/pr11010268>

Received: 21 December 2022

Revised: 7 January 2023

Accepted: 10 January 2023

Published: 13 January 2023



**Copyright:** © 2023 by the authors. Licensee MDPI, Basel, Switzerland. This article is an open access article distributed under the terms and conditions of the Creative Commons Attribution (CC BY) license (<https://creativecommons.org/licenses/by/4.0/>).

**Keywords:** angle of repose; parameter calibration; irregular particles; multi-objective optimization; gravel

## 1. Introduction

At present, centrifugal slurry pumps, as crucial equipment for solid–liquid two-phase transport media, are widely used in many fields, such as in mining [1–3], iron and steel metallurgy [4], waterway dredging [5,6], etc. Due to the phenomenon that many solid particles of different properties interact with the pump in the medium transported by the centrifugal pump, the slurry pump has problems of high energy consumption, severe wear of flowing parts, poor equipment operation reliability, and so on [7]. At the same time, due to the complex mechanism of particle interaction in two-phase flow, the hydraulic design of centrifugal pumps is usually based on pure water conditions. In the actual production process, the lack of design ability to resist the erosion of solid particles further aggravates the problem of short pump life and low pump efficiency. Therefore, an in-depth study of the solid particle properties and the flow condition of the particles inside the centrifugal slurry pump is beneficial to improve its efficiency in industrial applications.

With the improvement in computational performance and the gradual study of the subject by researchers, the discrete element method (DEM) has become an efficient and promising analytical method for researchers to analyze the flow behavior of particles

and their interactions. The method is widely used, and has performed well in studies analyzing a wide range of bulk particle types, such as ores, soils, powders, etc. The core concept of DEM is to simulate natural materials using a finite number of different elements to simulate the physical behavior of the particle flow by correctly defining the microscopic parameters that affect the macroscopic behavior of the material. For non-viscous bulk materials, these parameters usually include particle shape, size distribution, particle density, contact stiffness, friction coefficient (sliding and rolling), and damping coefficient (collision recovery coefficient). Determining these parameter values directly affects the macroscopic behavior of the material. Since there is no computational method to obtain the parameter values of the system response directly, it is necessary to calibrate the DEM model parameters. Generally speaking, DEM simulation parameters are mainly obtained by direct measurement calibration, indirect virtual calibration, or a combination of both. A few parameters that are easy to measure can be directly obtained from experimental measurements for accurate results. However, the measurement results obtained by direct observation vary significantly due to the influence of the particle material's properties and the limitations of the experimental method. Therefore, the results of the above parameter measurements usually cannot be directly applied to the DEM numerical simulation.

In recent years, many researchers have used virtual simulation experiments to calibrate the DEM parameters required for DEM simulations, and extensive research has been conducted for this purpose. Most of these calibration methods use the "trial and error method," which consumes a lot of experimental time for repeated parameter testing and is computationally expensive. To make the calibration process more efficient, many researchers have tried to reduce computational costs while obtaining better expected results by building predictive models and optimizing algorithms. For example, Ma et al. [8] developed a calibration model between the macroscopic parameters of rockfill materials and the microscopic parameters of the contact model (bonding contact model) using a relevance vector machine and a memetic algorithm. They verified the feasibility of the calibration model using a numerical triaxial test. Benvenuti et al. [9] performed a parameter calibration of cohesionless sintered ores using standard random distribution sampling and artificial neural networks. The calibration results were checked by angle of repose tester experiments to obtain the DEM parameters to be calibrated. Hesse et al. [10] proposed a new calibration for interpreting the shape characteristics of granular materials using convolutional neural networks, which can derive the material's flow and stacking behavior. The method was verified to have good predictive robustness by silo experiments. Wang et al. [11] developed an improved PSO calibration method, which is automated by a python script to simplify the calibration process significantly, and proved to be efficient and effective by comparing with experimental results. Nasato et al. [12] used artificial neural networks combined with the coarse-grained concept to calibrate the contact parameters of complex-shaped particles. The method's effectiveness was confirmed by predicting the static and rolling friction of the particles using void fraction and dynamic angle of repose, combined with experimental results for octahedral and cubic-shaped particles. He et al. [13] proposed a powder calibration method based on the genetic-algorithm-optimized BP neural network. The range of input parameters was obtained by a search algorithm with cluster analysis and combined with actual experiments. It was experimentally verified to be an efficient calibration method. Degrassi et al. [14] used DEM to numerically simulate the diffusion behavior of coke particles in a blast furnace. They calibrated the contact parameters of the particles using a meta-model algorithm and verified the model's accuracy by comparing it with actual blast furnace plant visualization data. Richter et al. [15] proposed a procedure to calibrate non-cohesive bulk particles' contact parameters, combining experiments, numerical simulations, and optimization algorithms. A new generalized surrogate-model-based optimization algorithm was used to calibrate the contact parameters of particles using coarse gravel as a research object. The comparison with experimental results showed that the algorithm is an effective way. Some researchers have retained the study on underlying physical contact laws during the calibration process, and have developed new

efficient calibration frameworks for this purpose. Qu et al. [16,17] proposed a hybrid analytic–computational method to calibrate the contact stiffness of particles. The initial estimate of contact stiffness is obtained using a derived semi-analytical and semi-empirical formula in the article. Reliable numerical estimates between macroscopic parameters and microscopic targets have been obtained by combining the gradient descent method, and verified by case studies. In the calibration process of Hertz-type contact parameters based on this framework, the machine learning algorithm Adam has been introduced for optimization, and obtained more efficient and accurate results. In addition, Qu et al. [18] proposed a strain-energy-based method for the calibration of elastic parameters of solid materials. The method is based on the idea of decoupling and minimizing the difference in strain energy between the discrete and continuum systems, which significantly improves calibration efficiency and application flexibility. The above research has significantly improved the efficiency and accuracy of the calibration process and facilitated the progress of parameter calibration.

In addition, in the current DEM simulation, many researchers simplify the shape of the simulated particles to a spherical shape for the calculation to improve computational efficiency. However, the fact is that most particles are not perfectly spherical. The volume friction of irregularly shaped particles when assembled compared to standard spherical particles is usually lower [19], which can affect the DEM calculation of contact force to produce bias [20], leading to a significant difference in the actual results. Some researchers have found that increasing the complexity of the particles is beneficial to improving the local curvature of the particles and reducing the computational error in calculating the contact force [21]. Barrios et al. [22] used single-particle tests to estimate material and contact parameters, showing that particles have reasonable physical significance only when modeled as natural shapes. In addition to this, the study of irregularly shaped particles (including particle shape and geometric behavior, etc.) is of tremendous research importance in many industrial processes; for example, some researchers have found that the shape of the particles has a significant effect on the mixing, filling, and wear of the material. Li et al. [23] constructed a model of iron ore particles with the multi-sphere clump method. They found that iron ore particles are highly irregular, and reducing them to spherical particles is inappropriate. Xu et al. [24] used DEM to study the wear of non-spherical ores on parts of tumbling mills, and found that the wear caused by cuboid-like particles was significantly larger than that caused by spherical particles. Tang et al. [25] compared the wear produced by four different-sphericity particles with spherical particles on the flow parts of a centrifugal pump. The results showed that the overall impact wear rate of the flowing components of the centrifugal pump showed a trend initially decreasing and then increasing with increasing sphericity, while the overall abrasive wear rate has been growing steadily. Therefore, a suitable geometry of irregular particles should be selected when simulating solid particles to accurately describe the shape of solid particles inside the centrifugal slurry pump and reduce costs.

Therefore, based on the summary mentioned above and given that the solid particles in this study are mostly bulk irregular gravels, this paper combines various concepts for the multi-objective optimization of the parameter calibration of irregular gravels. First, an appropriate filled model is obtained by modeling the actual particle 3D scan model using the fast multi-sphere method. Literature references and experimental measurements determine the material's most sensitive contact parameters, and the sample space is obtained by sampling using the LHS method. The calibration process is accomplished by baffle lifting tests, rotary drum tests, and simulation. Then, the RBF neural network is used to construct a surrogate model between the microscopic contact parameters and the macroscopic angle of repose. The optimal combination of DEM parameters is determined by NSGA-II and verified by hollow cylinder lifting tests. Finally, the corresponding numerical simulations based on the above calibration parameters are carried out to verify the feasibility of the parameter combinations' application. The method will provide a reference basis for the experimental study of centrifugal pump simulation.

## 2. Materials and Methods

### 2.1. The Measurement Method of Angle of Repose

#### 2.1.1. The Angle of Repose Measurement Setup

In this work, 25/10 mm dry gravel samples are selected as the experimental test material, which is a common material in the actual production process of the centrifugal slurry pump studied in this case, and the material is easily accessible in a non-viscous and free-flowing state. To comprehensively evaluate the performance of the calibration frame, the static angle of repose and the dynamic angle of repose of the material are measured and calibrated using the baffle lifting test and the rotary drum test, respectively, in this experimental test study.

##### (1) Baffle testing setup

The baffle lifting test setup is shown in Figure 1. The structure consists of three parts: three fixed Plexiglas walls, a Plexiglas substrate, and a sliding baffle. The test setup's length, width, and height are 300 mm, 200 mm, and 400 mm, respectively. The dimensions of these rectangular plates should be chosen to be large enough to reduce the wall effect on the angle of repose of the test study. A fixed mass of gravel is transferred into the box in the experiment. After forming a relatively flat material surface, the baffle is lifted at a constant speed of 0.1 m/s to allow the gravel to flow freely out of the box until it stabilizes, forming a slope of the material. The angle of this slope is called the static angle of repose, and the angle value can be obtained using image processing.

##### (2) Rotary drum test setup

The rotary drum experimental setup is shown in Figure 2. The drum is made of Plexiglass, with an inner diameter of 300 mm and a length of 150 mm. According to the results of Arntz [26], when the fill level of the material exceeds 65%, severe radial segregation occurs; therefore, in this experimental study, the total fill mass of the sand and gravel material is controlled to 40% of the maximum particle fill level. Then, the rotation starts at a uniform speed of 30 rpm. After the particle flow is stabilized, the angle between the particle surface and the horizontal plane is measured as dynamic angle of repose.

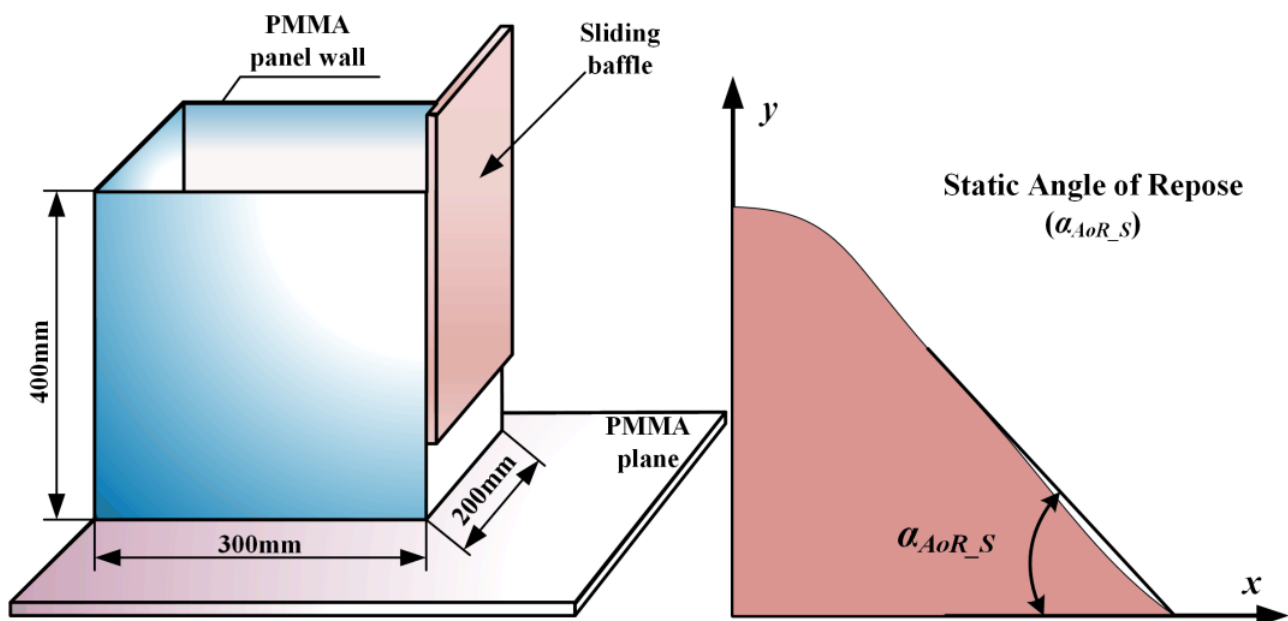
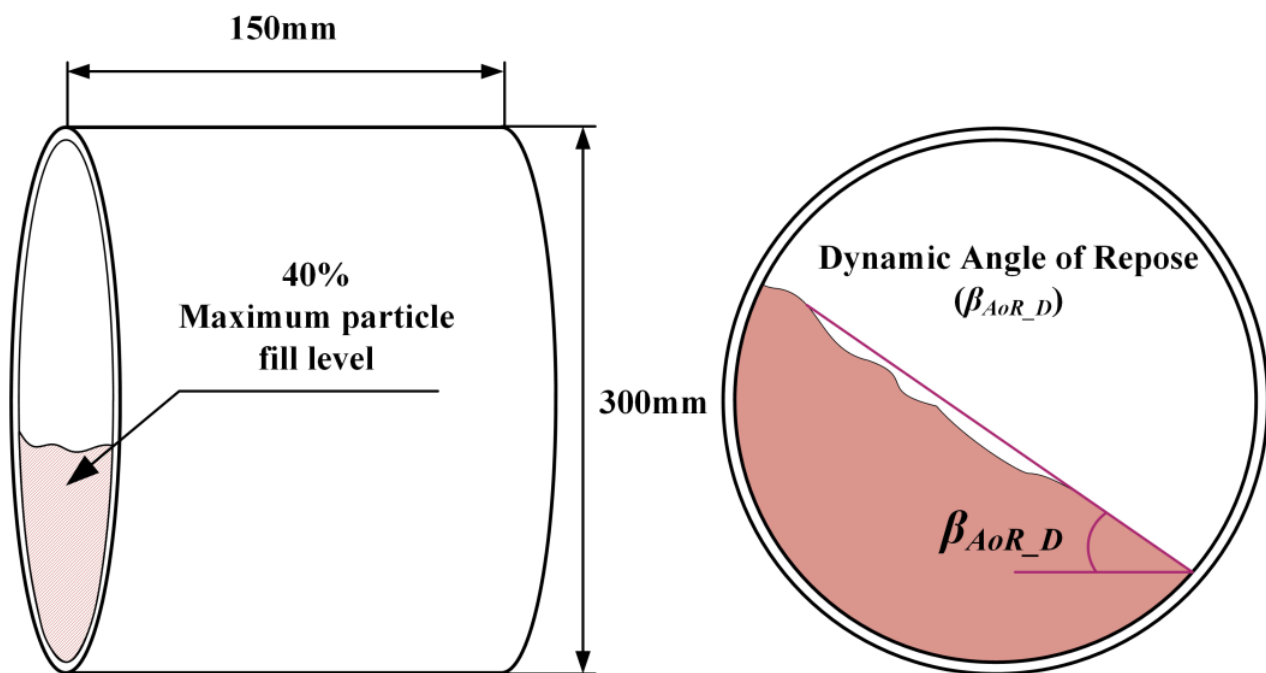


Figure 1. Principles of the baffle lifting test.



**Figure 2.** Principle of the rotary drum test.

### 2.1.2. The Measurement Method of Angle of Repose Value

The angle of repose is formed by the natural accumulation of granular materials under unconstrained conditions, which is commonly used as a macroscopic response parameter to characterize the specificity of the particles. When materials pile up in a horizontal plane to form a non-collapsing slope [27], the microscopic parameters of the material can be measured indirectly from this macroscopic response, and the angle of this slope is the material's angle of repose.

In acquiring the material's angle of repose, the commonly used method is to capture the image information formed by accumulating granular materials using a high-resolution camera, and then process the image using computer image processing technology. The general image processing stage includes grayscale, binarization, denoising, edge point extraction, and least squares linear fitting of edge points. The angle of repose value can be calculated based on the slope of the fitted straight line. This paper shows the specific image processing strategy for the static angle of repose test in Figure 3a–d.

The dynamic angle of repose was obtained by high-resolution processing video of the drum rotation taken by a high frame rate camera. The dimensions and setup of the test are as described in Section 2.1.1. Recording started when the drum began to rotate, and a total of 30 s of the experimental video was recorded, corresponding to 15 revolutions of the drum. To ensure that the data recorded are not affected by changes in the surface of the initial drum particles, the data after five revolutions of the drum are used as the final test record. The captured video is converted into image data, and a square area with a length equal to half of the drum diameter is cropped near the drum's center, then, the image is captured [28]. The selection result of the clipped area is shown in Figure 4a. This experimental work selects the start–middle–end moment image data corresponding to each drum revolution for processing. The free contour of the material surface in the clipped area is obtained by image processing, as shown in Figure 4b–d shows the average surface profile obtained from the experimental image corresponding to 10 revolutions of the drum. The average slope is obtained by linear fitting based on the acquired surface profile position data. This paper takes the arctangent value of this average slope to the horizontal plane as the dynamic angle of repose.

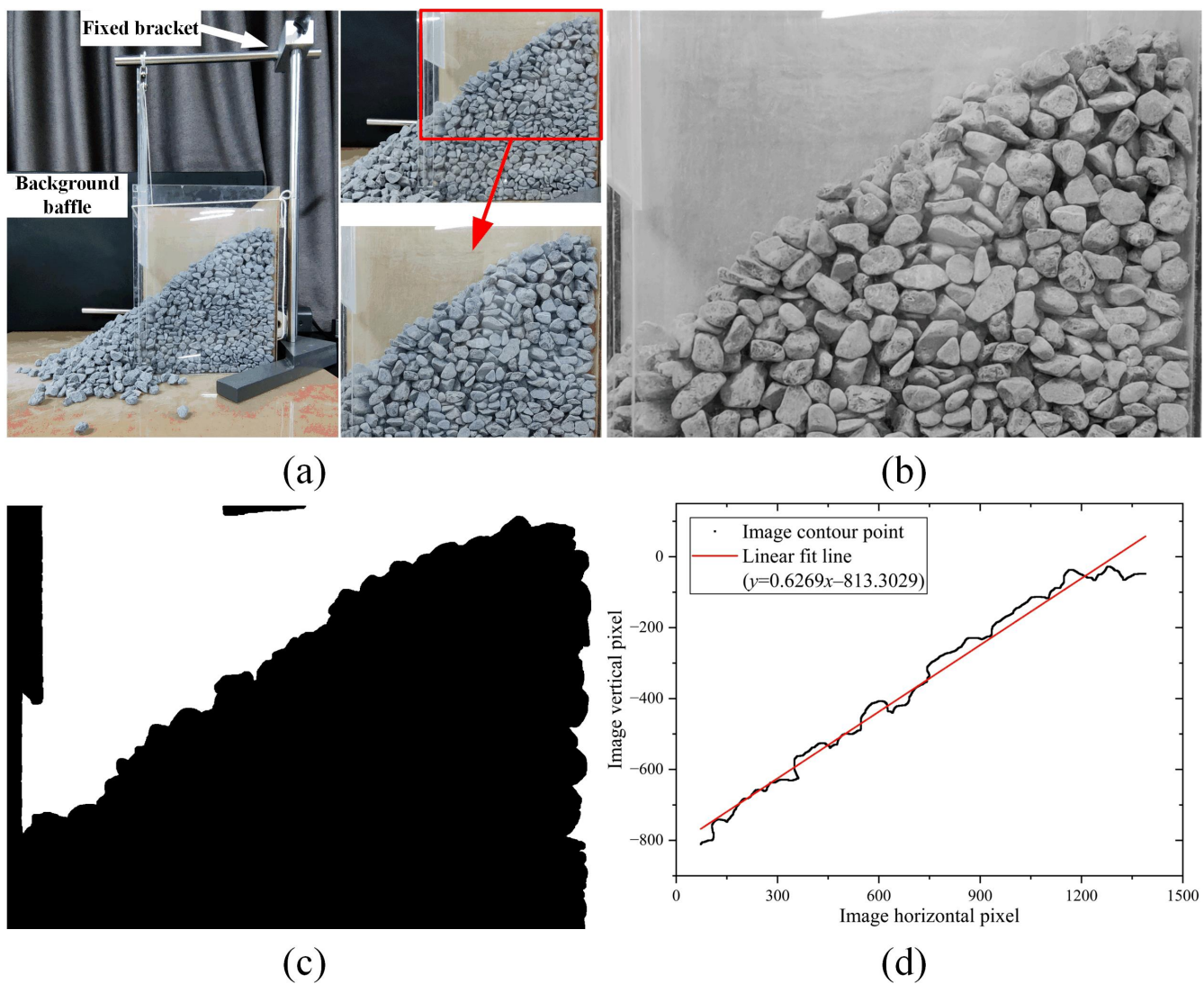


**Figure 3.** Measurement process of static angle of repose: (a) original image; (b) grayscale image; (c) binarized image; (d) linear fitting image.

Repeatability tests were conducted for both types of experiments mentioned above, and the results of the experimental process are shown in Table 1.

**Table 1.** Experimental results of the angle of repose.

Test Sequence	Baffle Lift Test (Static Angle of Repose Test)		Rotary Drum Test (Dynamic Angle of Repose Test)		
	Linear Fit Slope Value	Angle Value (°)	Mean Value of $\alpha_{AoR_S}$ (°)	Mean of Linear Fit Slope	Mean Value of $\beta_{AoR_D}$ (°)
1	0.6515	33.0834	32.5340	1.1527	49.0579
2	0.6292	32.1781			
3	0.6448	32.8131			
4	0.6269	32.0852			
5	0.6373	32.5102			

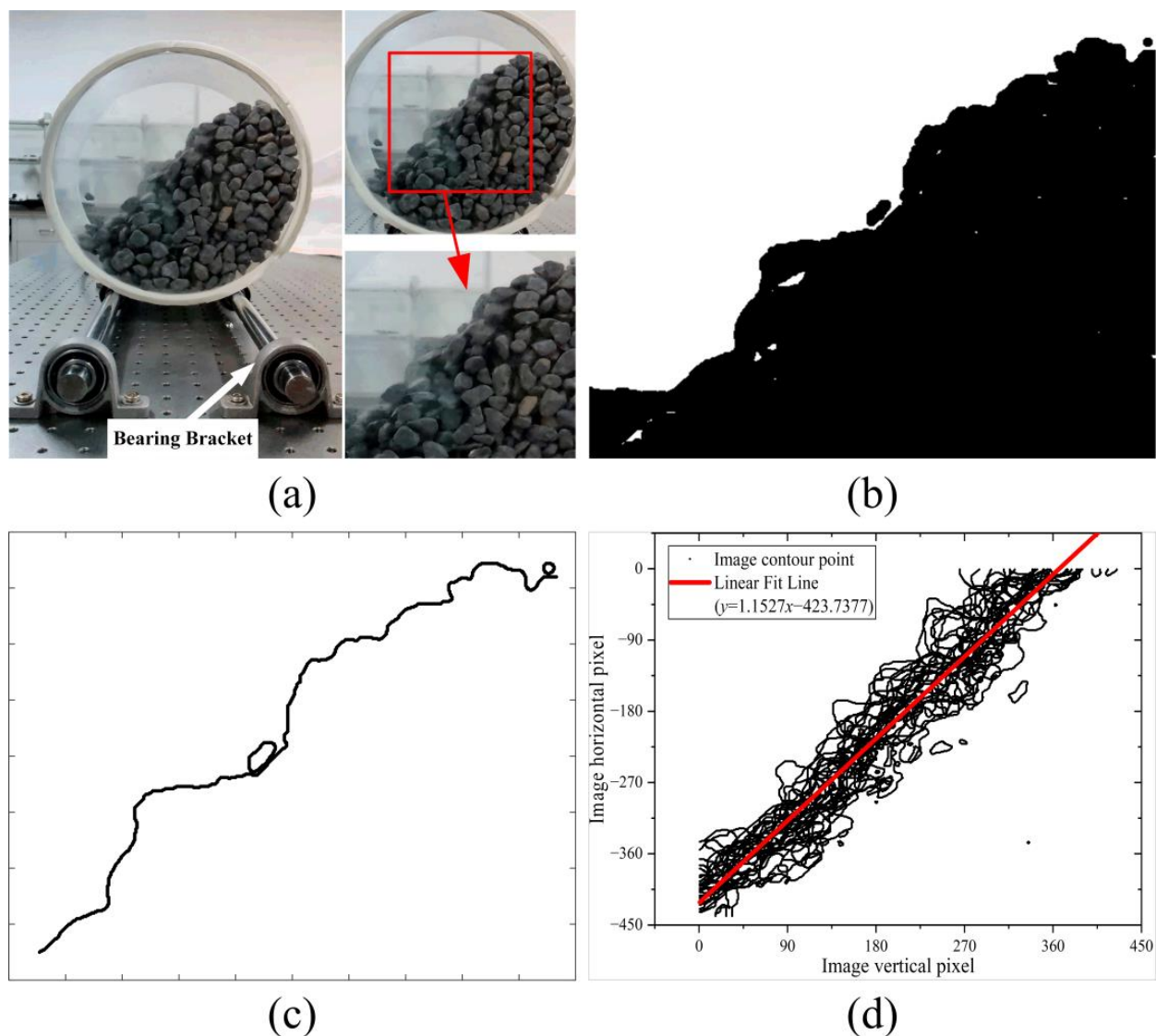


**Figure 4.** Measurement process of dynamic angle of repose: (a) acquisition of clipped area; (b) binarized image; (c) contour image; (d) average linear fit image.

## 2.2. DEM Contact Model

In this paper, to accurately describe the flow state of dry sand and gravel materials, the simulation was performed using a Hertz–Mindlin (no-slip) model built in the commercial DEM software EDEM (EDEM 2020, DEM Solutions, Edinburgh, UK). The Hertz–Mindlin no-slip model is one of the essential contact models in DEM simulations [29], as shown in Figure 5, which combines the Hertz contact theory with Mindlin’s improved part of the tangential no-slip model, and it can accurately calculate the contact forces between the pellets.

The normal contact force  $F_n$  for the contact between particle A and particle B can be described as

$$F_n = \frac{4}{3}E^*\sqrt{R^*}\delta_n^{\frac{3}{2}} \quad (1)$$

where  $\delta_n$  is the normal overlap,  $E^*$  is the equivalent Young’s modulus, and  $R^*$  is the equivalent radius.  $E^*$  and  $R^*$  can be defined as

$$\frac{1}{E^*} = \frac{(1 - \nu_A^2)}{E_A} + \frac{(1 - \nu_B^2)}{E_B} \quad (2)$$

$$\frac{1}{R^*} = \frac{1}{R_A} + \frac{1}{R_B} \tag{3}$$

where  $E_A, \nu_A, R_A, E_B, \nu_B,$  and  $R_B$  are the Young’s modulus, Poisson’s ratio, and contact sphere radius of contact body A and contact body B, respectively.

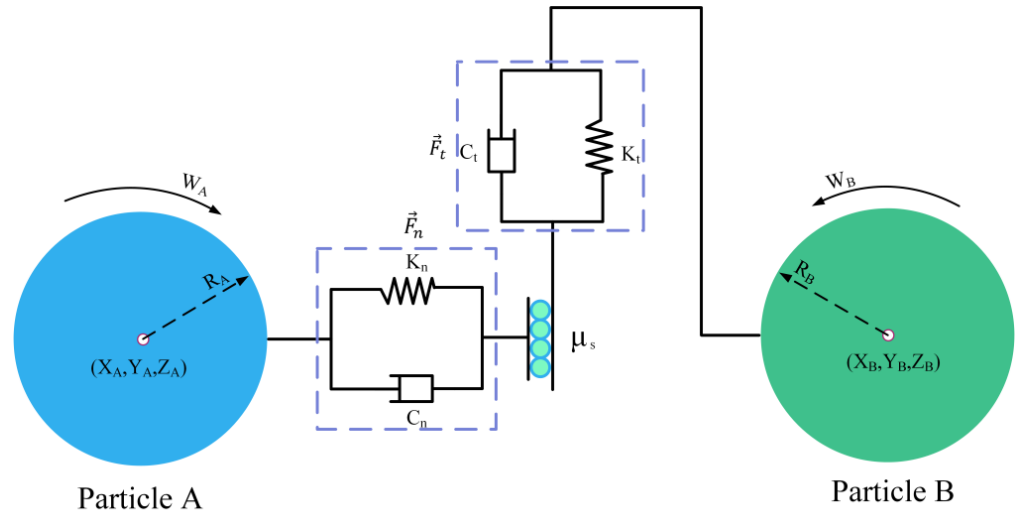


Figure 5. Contact mechanics model between the particles.

The tangential contact force  $F_t$  between particle A and particle B is related to the tangential overlap  $\delta_t$  and the tangential stiffness  $S_t$ . The tangential force can be described as

$$F_t = -\delta_t S_t \tag{4}$$

The tangential damping force is defined as

$$F_t^d = -2\sqrt{\frac{5}{6}}\beta\sqrt{S_t m^*} v_t^{rel} \tag{5}$$

where  $v_t^{rel}$  is the tangential component of the relative velocity between the two contacting bodies of A and B. The tangential stiffness  $S_t$  is defined as

$$S_t = 8G^* \sqrt{R^* \delta_n} \tag{6}$$

where  $G^*$  is the equivalent shear modulus, which can be described as

$$G^* = \frac{1}{G_A} + \frac{1}{G_B} \tag{7}$$

where  $G_A$  and  $G_B$  are the shear modulus of contact bodies A and B, respectively. Considering that the granular material applied in this paper is a non-viscous bulk material, the tangential force will be limited by Coulomb friction ( $\mu_s F_n$ , where  $\mu_s$  is the coefficient of static friction). To ensure the accuracy of the tangential force calculation in the calculation process, therefore, the tangential force [30] is defined in this paper as

$$|F_t| = \min \left\{ \left| F_t^p - k_t \Delta \delta_t \right|, \left| \mu F_n \right| \right\} \tag{8}$$

where  $k_t$  is the tangential stiffness of the contact,  $F_t^p$  is the tangential force at the previous time step,  $\Delta \delta_t$  is the incremental tangential displacement between the two particles, and  $\mu$  is the friction coefficient.

The normal damping force  $F_n^d$  between particle A and particle B can be described as

$$F_n^d = -2\sqrt{\frac{5}{6}}\beta\sqrt{S_n m^*} v_n^{rel} \quad (9)$$

where  $v_n^{rel}$  is the normal component of the relative velocity between the contacting bodies, and  $m^*$ ,  $\beta$ , and  $S_n$  denote the equivalent mass, damping ratio, and normal stiffness, respectively, and can be defined as

$$G^* = \frac{1}{G_A} + \frac{1}{G_B} \quad (10)$$

$$\beta = \frac{\ln e}{\sqrt{\ln^2 e + \pi^2}} \quad (11)$$

$$S_n = 2E^* \sqrt{R^* \delta_n} \quad (12)$$

where  $m_A$  and  $m_B$  express the masses of contact bodies A and B, respectively, and  $e$  is the coefficient of recovery.

### 2.3. Particle Property Parameters

When performing DEM material parameter calibration, the material parameters studied can be divided into two categories: those obtained from direct measurements and those obtained from DEM simulations. The following requires the study of each of these two types of property parameters.

#### 2.3.1. Measurement of Direct Particle Parameters

##### (1) Irregular-shaped particle modeling

As mentioned in Section 1, the particle shape can significantly impact the DEM calibration accuracy and fluidity studies. Therefore, to ensure the accuracy of the DEM simulation, the gravel particle shapes are divided into five categories: cone, prism, discoid, ellipsoid, and sphere. Various typical particles are selected to generate 3D digital mesh models using a high-precision 3D scanner. Then, the geometric models used for DEM simulations are generated in the discrete element simulation software with the particle filling tool. The constructed multi-sphere model is shown in Figure 6, and the relevant parameters are shown in Table 2.

Table 2. Model parameters for different fill levels.

Particle Shape	Low Fill Level (5~8 Spheres)			Medium Fill Level (20~25 Spheres)			High Fill Level (40 + Spheres)		
	Number	Volume ( $\times 10^3 \text{ mm}^3$ )	Mass (g)	Number	Volume ( $\times 10^3 \text{ mm}^3$ )	Mass (g)	Number	Volume ( $\times 10^3 \text{ mm}^3$ )	Mass (g)
Cone	5	3.83	10.19	24	4.68	12.47	46	4.63	12.32
Prism	6	5.56	14.85	22	6.50	17.29	42	6.83	18.19
Discoid	5	0.48	1.28	23	1.18	3.14	44	1.33	3.53
Ellipsoid	8	1.67	4.44	22	1.84	4.91	42	1.93	5.14
Sphere	5	1.89	5.02	25	1.89	5.04	43	1.81	4.81

As seen in Figure 6, the gap between the actual model and the filled model due to sharp edges gradually decreases as the filling level increases, gradually increasing the filling accuracy between the filled model and the original model. In this paper, the relative volume error of the model is used to quantify the error between the particle-filled model created by the multi-sphere method and the actual model, and the relative volume error  $V_{re}$  is described as

$$\text{Relative volume error} = \left| \frac{V_m - V_R}{V_R} \right| \times 100\% \quad (13)$$

where  $V_m$  is the filled model volume and  $V_R$  is the actual particle volume. The model volume and relative volume errors for the above different fill levels are shown in Figure 7. From the figure, it can be seen that although using more and smaller spheres can reduce the relative volume error to improve the accuracy of the fitted model, at the same time, it also increases the computational cost significantly. Therefore, a medium fill level (20~25 spheres) is finally chosen for DEM model construction to improve the computational efficiency.

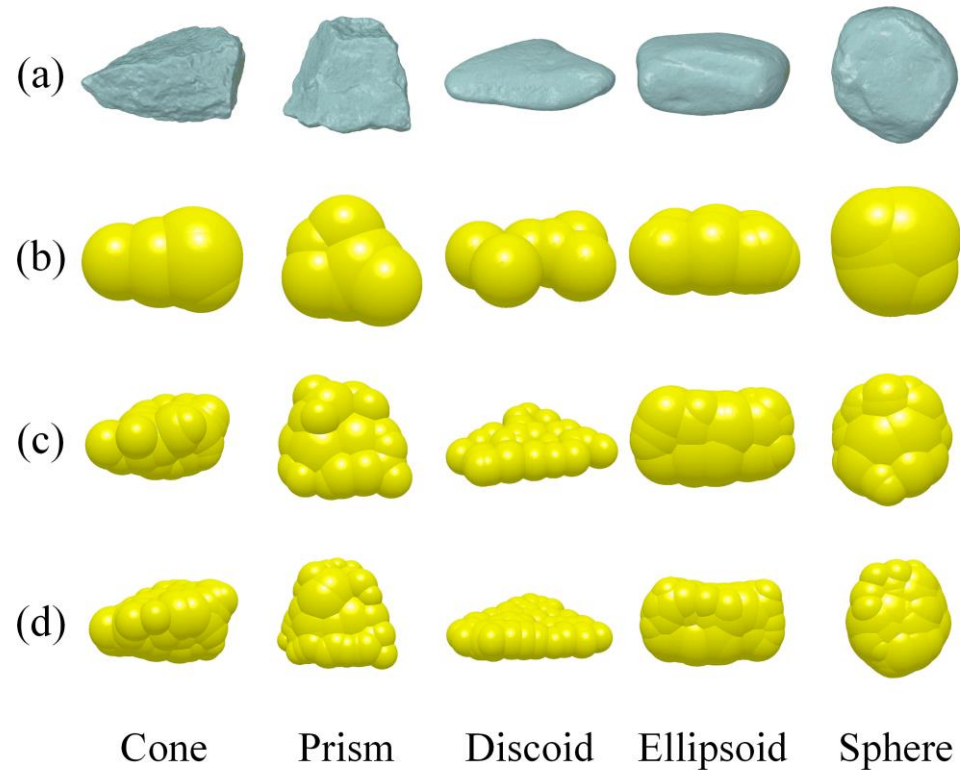


**Figure 6.** Particle category: (a) original 3D scanned model; (b) low fill level; (c) medium fill level; (d) high fill level.

Standard sampling of 1 L particles was carried out according to the above particle shape classification; Table 3 shows the percentage of the number of particles of different shapes. When performing DEM simulations, the number of particles is controlled according to the statistical ratio of the number of particles.

**Table 3.** Model parameters for different fill levels.

Particle Shape	Cone	Prism	Discoid	Ellipsoid	Sphere
Percentage (%)	18.61	23.73	22.65	18.11	16.90

Meanwhile, in order to describe the closeness of the irregular particle geometry to a perfect sphere, the sphericity [31] is used to define as

$$\Psi = \frac{SA_{es}}{SA_{rp}} = \frac{\sqrt[3]{36\pi V^2}}{SA_{rp}} \quad (14)$$

where  $SA_{rp}$  is the actual surface area of the particle,  $\text{mm}^2$ ;  $SA_{es}$  is the surface area of the sphere determined from the same volume of particles,  $\text{mm}^2$ ; and  $V$  is the actual volume of the particle,  $\text{mm}^3$ . As described in the previous section, the final model parameters for constructing the DEM simulation model of irregular particles using the fast multi-sphere method are shown in Table 4.

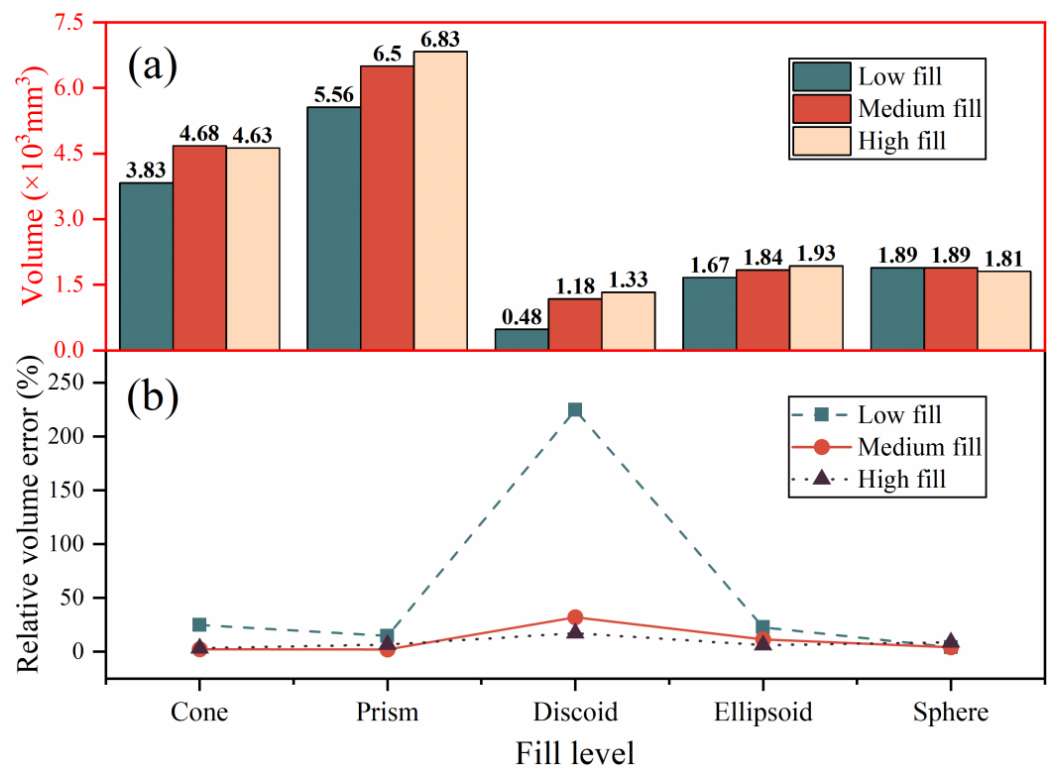


Figure 7. Particle performance at different fill levels: (a) fill volume; (b) relative volume error.

Table 4. Model parameters for different fill levels.

Type	$SA_{rp}$ ( $\text{mm}^2$ )	$SA_{es}$ ( $\text{mm}^2$ )	$V_R$ ( $\text{mm}^3$ )	$V_m$ ( $\text{mm}^3$ )	$\Psi$	$V_{re}$ (%)
Cone	1709.798	1325.839	4.782	4.540	0.775	5.07
Prism	2027.787	1742.317	6.373	6.839	0.859	7.30
Dicoid	873.751	573.521	1.558	1.292	0.656	17.08
Ellipsoid	874.393	725.863	2.048	1.839	0.830	10.21
Sphere	758.346	727.244	1.767	1.844	0.959	4.36

## (2) Apparent density measurement of particles

In this paper, the apparent density of irregular particles was measured using the fluid displacement method. The mass of the particles was determined by a mass gauge (0.01 g accuracy). The material was poured into a graduated cylinder (205 mm diameter and 1000 mL volume) for 1 min. Then, the difference in the volume change in the fluid inside the cylinder was measured. Due to the low porosity of the experimental material, the liquid volume change in the internal permeation of the particles is ignored to simplify the testing procedure. In addition, to show that the angle of repose measured by the above method is not significantly affected by changes in permeate volume, we conducted a sensitivity analysis on particle density and angle of repose, described in Section 2.3.2. The particle's apparent density is the ratio of the difference in volume between the material's mass and the change in liquid. The measurements were repeated 10 times to ensure the experiment's reliability, and the results are shown in Table 5.

### 2.3.2. Sensitivity Analysis of Particle DEM Parameters

In this section, the influence of the characteristic intrinsic parameters of the particles (Young's modulus, Poisson's ratio, particle density, collision recovery coefficient) on the angle of repose is studied and analyzed. The results are shown in Figure 8. The value

or range of contact parameters of particle–particle, and particle–geometry interactions in DEM calibration are provided, as shown in Table 6.

**Table 5.** Apparent density measurement of particles.

No.	Volume of Replacement Liquid (mL)	Mass (g)	Apparent Density (g/mL)	Mean Value (g/mL)	Standard Deviation
1	9.5	25.703	2.706		
2	17.0	44.750	2.632		
3	9.4	25.447	2.707		
4	18.0	47.883	2.660		
5	13.5	35.407	2.623		
6	14.2	37.047	2.609	2.661	0.052
7	14.2	38.300	2.697		
9	13.5	35.087	2.599		
9	6.0	16.580	2.763		
10	8.0	20.940	2.618		

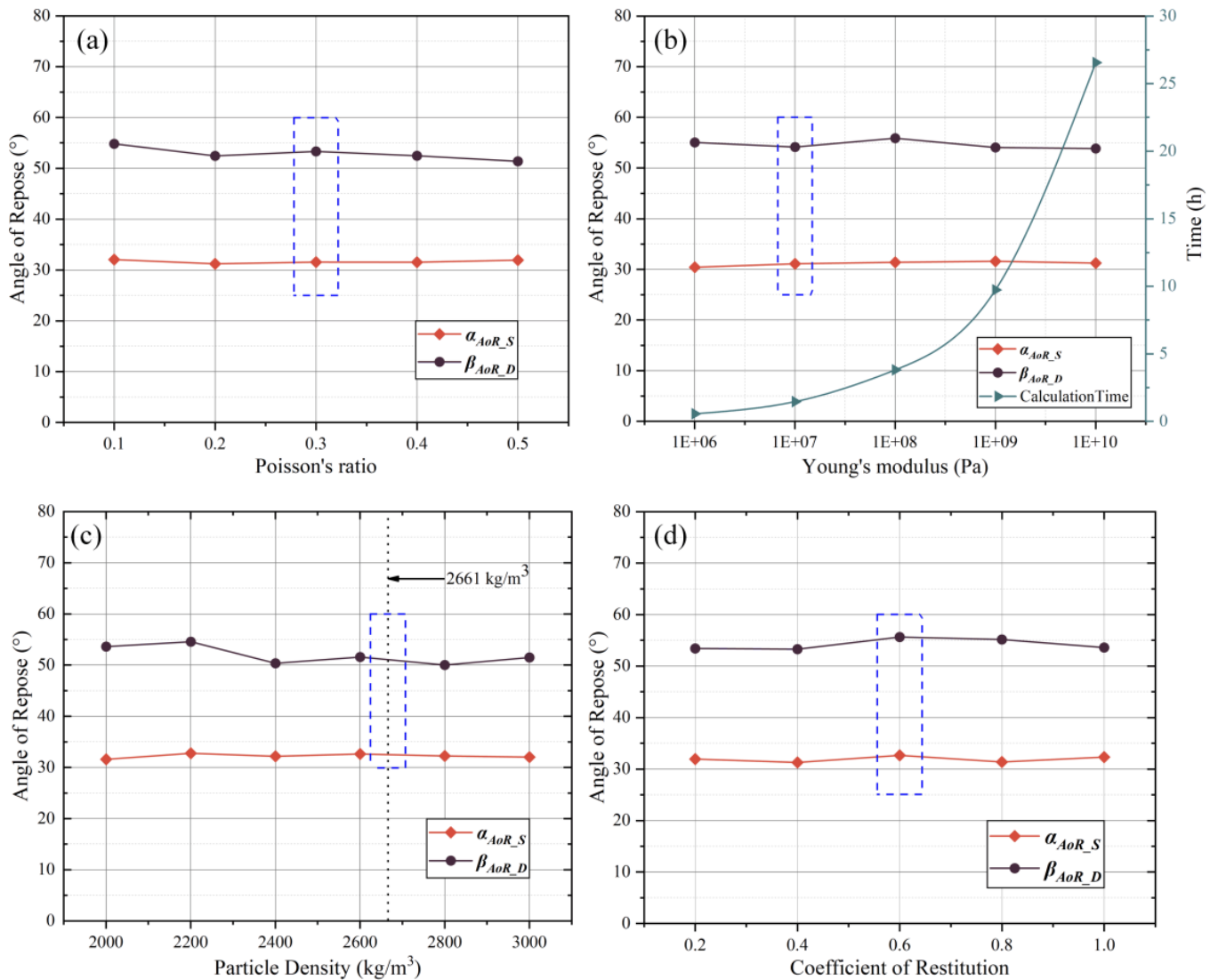


**Figure 8.** Particle intrinsic parameters: (a) Poisson’s ratio; (b) Young’s modulus; (c) particle density; (d) coefficient of restitution.

**Table 6.** DEM parameters, relevant symbols, and values/ranges studied in this paper; parameters to be calibrated are set as ranges, which are denoted by \*.

DEM Parameters	Symbol	Value/Range	Source
Plexiglass Poisson's ratio	$\nu_w$	0.25	Literature [21]
Shear modulus of Plexiglass (Pa)	$G_w$	$3 \times 10^9$	Literature [21]
Plexiglass density (kg/m <sup>3</sup> )	$\rho_w$	1190	Literature [21]
Particle Poisson's ratio	$\nu_p$	0.3	Section 2.3.2
Particle Young's modulus (Pa)	$G_p$	$1 \times 10^7$	Section 2.3.2
Particle density (kg/m <sup>3</sup> )	$\rho_p$	2661	Section 2.3.2
Collision recovery coefficient	$e$	0.6	Section 2.3.2
Particle–particle sliding friction coefficient	$\mu_{s\_pp}$	0–0.8 *	
Particle–particle rolling friction coefficient	$\mu_{r\_pp}$	0–0.8 *	
Particle–geometric sliding friction coefficient	$\mu_{s\_pw}$	0–0.8 *	
Particle–geometric rolling friction coefficient	$\mu_{r\_pw}$	0–0.8 *	
Rayleigh time step(s)	$\Delta t$	$4.2 \times 10^{-5}$	

Poisson's ratio and Young's modulus of particles are the critical parameters used to characterize the elastic properties of granular materials, and play an essential role in the study of deformation, fragmentation, and stress distribution of granular materials [28]. However, these parameters do not significantly affect the analysis of the macroscopic response of materials [32]. As shown in Figure 8a,b, it is evident that Poisson's ratio and Young's modulus have little effect on the static/dynamic angle of repose of the material. The influence of Poisson's ratio and Young's modulus on the material's static/dynamic angle of repose is minimal. With the increase in Poisson's ratio and Young's modulus, the average value of the change in the angle of repose is within 1.5°, but the calculation time shows an exponential increase. Based on the calculation cost and accuracy requirements, the parameters in this paper were chosen to be Poisson's ratio value of 0.3 and Young's modulus of  $1 \times 10^7$  Pa.

In Section 2.3.1, the density of the particles was measured directly. The relationship between the particles' density and the repose angle was also studied in this section to verify the method's reliability. Figure 8c shows that the static/dynamic angle of repose of the particles did not change significantly with the density change in a more extensive range of particle density change (2000–3000 kg/m<sup>3</sup>). The average change in the angle of repose of the particles in this range was within 2°. The overall error was about 3.5%; therefore, the method of ignoring the volume of liquid permeating inside the particles is appropriate in this paper. The final choice of particle density value is 2661 kg/m<sup>3</sup>.

In the static free-flowing case of gravel, the recovery coefficient also did not significantly affect the behavior of the particles. In this paper, different values of collision coefficients in the range of 0.2 to 1.0 were chosen for the above DEM simulations. The results presented in Figure 8d show that the collision coefficient has almost no effect on the angle of repose of the granular material in the simulation conditions set in this paper, which remains consistent with the conclusions obtained by other researchers [33]. The collision recovery coefficient was finally chosen to be 0.6 in this paper.

### 3. Construct the Optimal Mathematical Model

Relevant theories have shown that the combination of microscopic parameters affecting the granular material's macroscopic response is ambiguous when only a single calibration experiment is considered [34,35]. Therefore, this paper uses a multi-objective optimization model to study both the material's static and dynamic angle of repose and the flow chart of multi-objective optimization based on the RBF neural network and NSGA-II showed in Figure 9.

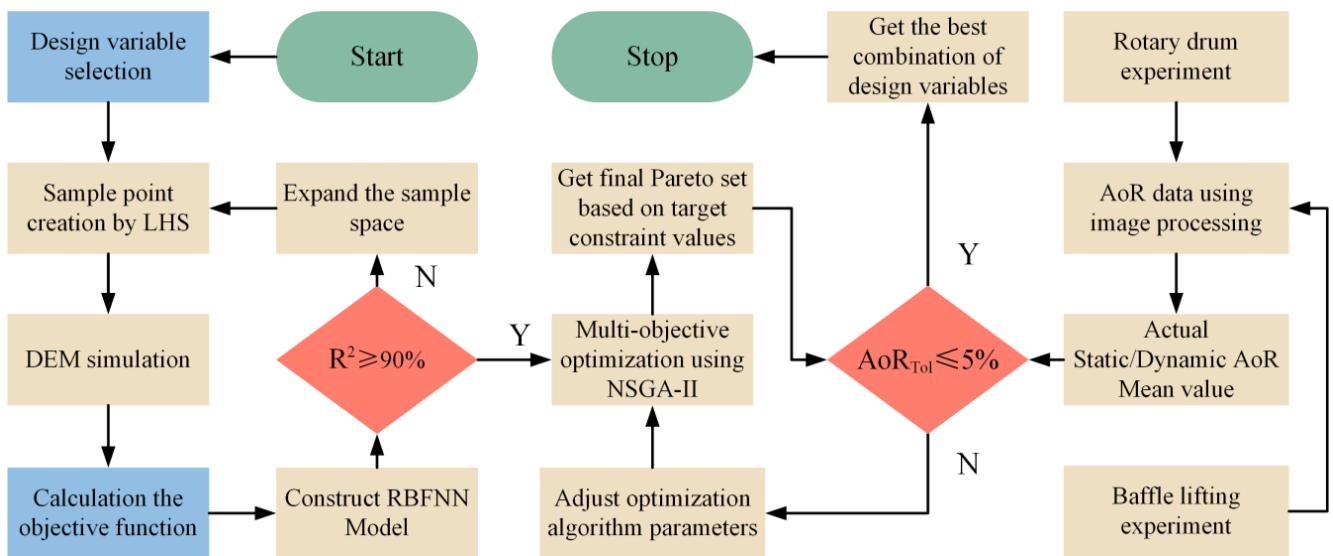


Figure 9. Flow chart of multi-objective optimization.

3.1. LHS-Based Model Dataset Construction

Optimal Latin hypercubic sampling is an improved method that enables the sampling points to be uniformly distributed inside the variable design space. Therefore, it has a good space-filling and equalization function.

This paper uses a uniformly distributed LHS-based method to sample the calibration parameters in multiple dimensions. The four DEM parameters ( $\mu_{s\_pp}$ ,  $\mu_{r\_pp}$ ,  $\mu_{s\_pw}$ ,  $\mu_{r\_pw}$ ) to be calibrated for the study were sampled in 140 groups to obtain a  $4 \times 140$  matrix of virtual test sample points. The first 100 groups are used as the RBF neural network training data, and the last 40 are used as the validation data. The sample point matrix constructed in this paper is shown in Table 7.

Table 7. Matrix of 140 sample points based on LHS sampling (partial data; full data in Appendix A).

No	Design Variables				Objective Functions	
	$\mu_{s\_pp}$	$\mu_{r\_pp}$	$\mu_{s\_pw}$	$\mu_{r\_pw}$	$\alpha_{AoR\_S}$	$\beta_{AoR\_D}$
1	0.177	0.329	0.533	0.427	28.3	54.1
2	0.585	0.582	0.469	0.273	37.1	66.6
3	0.599	0.441	0.796	0.342	40.6	66.8
			...			
138	0.220	0.647	0.107	0.623	18.3	21.8
139	0.678	0.744	0.026	0.762	7.9	17.5
140	0.031	0.658	0.126	0.684	8.1	22.1

3.2. RBF Neural Network Structure Design

The RBF neural network is a three-layer feed-forward neural network containing an input layer, a hidden layer, and an output layer. The first layer is the input layer, which includes all the design factors that produce the influence; the second layer is the hidden layer, where the nodes in the hidden layer use radially symmetric basis functions as activation functions [36,37]; and the third layer is the output layer, which is composed of all the responses. RBF neural networks transform the non-linear input–output mapping relationship into radial basis functions and the hidden layer–output layer transfer function into a linear adjustable function, which significantly accelerates the learning speed and avoids the local minimal value problem.

In this paper, the RBF neural network is used as an approximate model for fitting microscopic parameters (particle–particle and particle–geometric sliding/rolling friction coefficients) with macroscopic responses (static and dynamic angle of repose); the structure of the RBF neural network used in this paper is schematically shown in Figure 10.

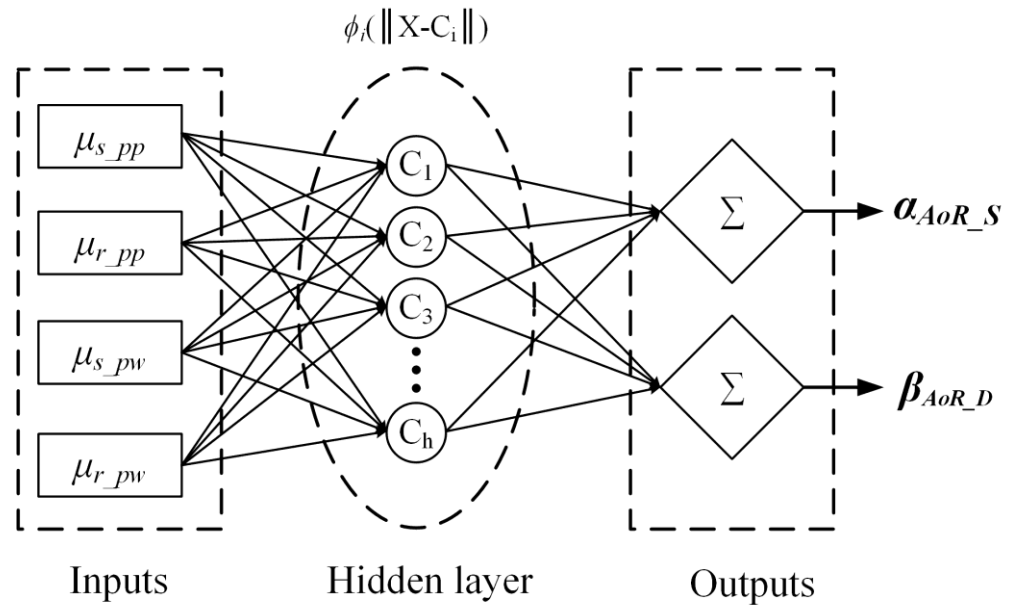


**Figure 10.** RBF neural network topology.

### 3.3. RBF Model Optimization Based on NSGA-II

This paper uses the NSGA-II algorithm to optimize the surrogate model above. The NSGA-II algorithm is a fast and efficient global optimization algorithm proposed by Kalyanmoy Deb in 2002 [38]. The algorithm ensures the diversity of populations with high precision optimization results by proposing a fast non-dominated sorting algorithm.

In this paper, the static/dynamic angle of repose values obtained from actual measurements of baffle lifting test and rotary drum test parameters are used as target constraints, while the design ranges of microscopic parameter variables are combined for optimization. The corresponding design variables and target function constraint equations are described as follows:

$$\begin{cases} \text{target value } \alpha_{AoR\_S} = 32.534^\circ \\ \text{target value } \beta_{AoR\_D} = 49.058^\circ \end{cases} \quad (15)$$

$$\text{Subject to } \begin{cases} 0 \leq \mu_{s\_pp} \leq 0.8 \\ 0 \leq \mu_{r\_pp} \leq 0.8 \\ 0 \leq \mu_{s\_pw} \leq 0.8 \\ 0 \leq \mu_{r\_pw} \leq 0.8 \end{cases} \quad (16)$$

## 4. Results and Discussion

### 4.1. Precision Analysis of RBF Model

The accuracy of the surrogate model is usually evaluated using the coefficient of determination  $R^2$  shown in Formula (17), which is also used to assess the RBF neural network surrogate model in this paper. When  $R^2$  is closer to 1, it proves a better fit for the model, which is usually considered in engineering applications when  $R^2 \geq 0.9$ .

$$R^2 = 1 - \frac{\sum_{i=1}^N (y_i - \hat{y}_i)^2}{\sum_{i=1}^N (y_i - \bar{y}_i)^2} \quad (17)$$

where  $y_i$  is the simulated value of the model;  $\hat{y}_i$  is the predicted value of the model;  $\bar{y}_i$  is the average of the simulated values of the model; and  $N$  is the number of sample points.

Figure 11 shows the linearly fitted static/dynamic angle of repose DEM simulated values versus predicted values, from which it can be seen that the regression coefficient  $R^2$  for the model is 0.965 for the static angle of repose and 0.958 for the dynamic angle of repose.

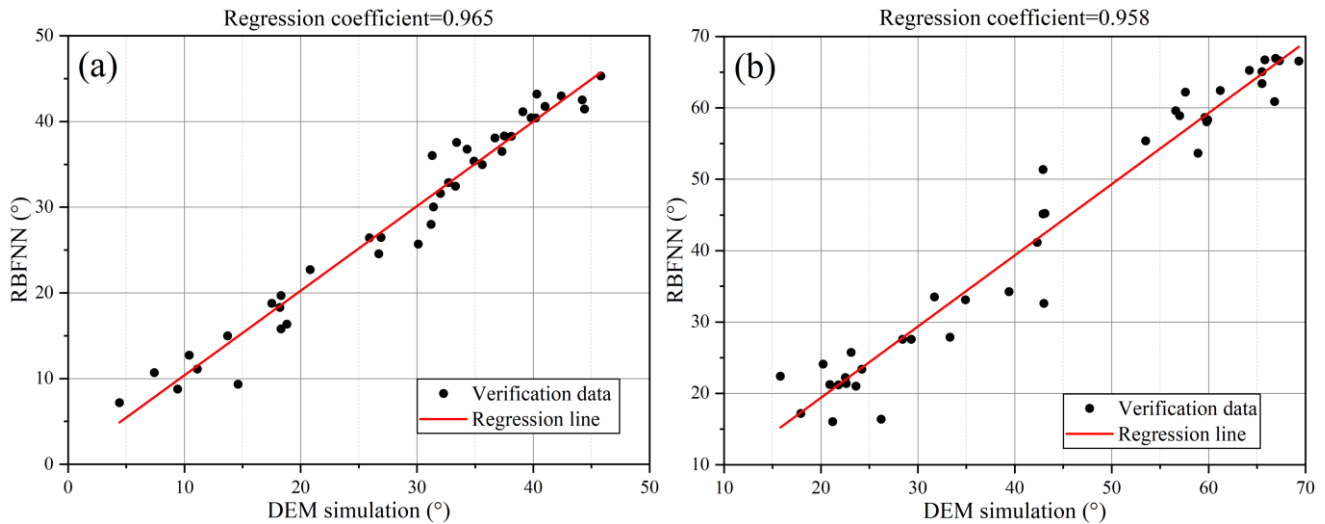


Figure 11. Validated solutions for 40 sets of objective functions: (a)  $\alpha_{AoR_S}$ ; (b)  $\beta_{AoR_D}$ .

In addition, We also analyzed the relative error between the angle of repose prediction value of the RBF model and the DEM simulation value. The results are shown in Figure 12, and there is only a small amount of dispersion between both. The predicted values of both targets are relatively close to the DEM simulation results; thus, it can be concluded that the established RBF neural network prediction model can be reliably calibrated for the DEM parameters.

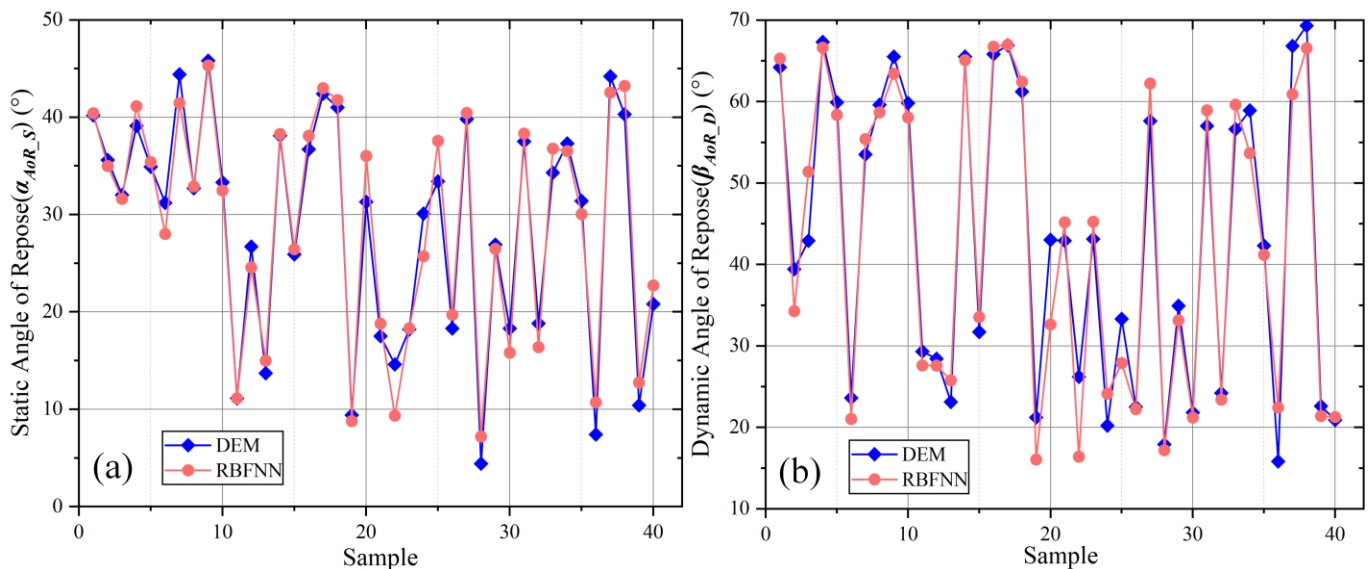
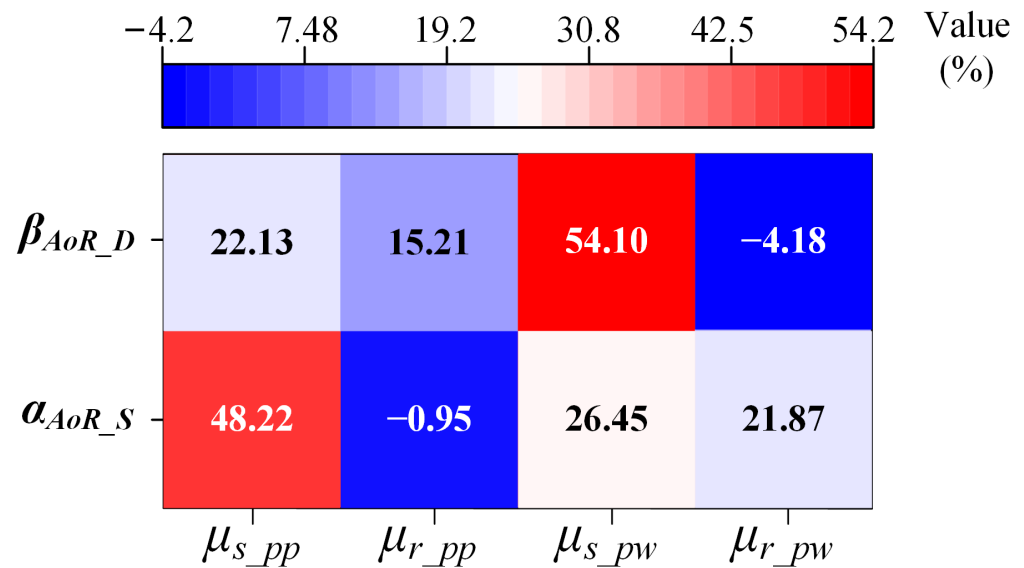


Figure 12. Relative error between RBFNN predicted and DEM simulated values: (a)  $\alpha_{AoR_S}$ ; (b)  $\beta_{AoR_D}$ .

The sensitivity analysis results are shown in Figure 13. It is evident that the particle–geometry static friction coefficient has the most significant effect on the dynamic angle of repose (54.10%). The particles have many frictional collisions with the geometry when they flow freely in the drum setup, so this coefficient significantly affects the dynamic

response angle. The particle–particle static friction coefficient is an essential factor that substantially affects the dynamic angle. In addition, the particle–particle static friction coefficient is a relevant variable that significantly affects the static angle of repose (48.22%). In summary, the static friction coefficient plays a crucial role in studying the performance of the macroscopic angle of repose of gravel particles.



**Figure 13.** Sensitivity diagram of the impacts of input variables on two objectives.

#### 4.2. Multi-Objective Optimization Design

In this work study, the meaning of multi-objective optimal design is to take the actual values of static/dynamic angle of repose ( $\alpha_{AoR\_S} = 32.054^\circ$ ,  $\beta_{AoR\_D} = 49.058^\circ$ ) obtained through experimental measurements as the objective constraint, and the particle–particle sliding friction coefficient, particle–particle rolling friction coefficient, particle–geometry sliding friction coefficient, and particle–geometry rolling friction coefficient as the optimization object, and find the optimal combination of parameters to satisfy the target results within the determined range of values of design variables. From the sensitivity analysis of parameters in Section 4.1, it can be seen that the objective functions are affected by each design variable to different degrees, so when dealing with the optimization problem of multi-objective parameters, the Pareto front is usually used as the solution to the optimization problem.

In this work, the relevant settings of the NSGA-II algorithm are shown in Table 8. The optimal combination of design variables obtained is the particle–particle sliding friction coefficient of 0.323, the particle–particle rolling friction coefficient of 0.061, the particle–geometry sliding friction coefficient of 0.316, and the particle–geometry rolling friction coefficient of 0.441. During the calibration of DEM parameters, it is almost impossible to achieve a perfect calibration match. This is mainly caused by two factors: (1) Parameter results, obtained through the laboratory, suffer from typical experimental scatters [39]. Meanwhile, to acquire different properties of particles, the results obtained from various experiments may also have conflicting problems, which dramatically affect the accuracy of calibration results. (2) Particle packing configuration in DEM simulation cannot be completely consistent with experiments. Therefore, some of the particles' behavior will inevitably be influenced by some random factors [40]. In summary, to guarantee the accuracy of simulation and experiment, it is reasonable to choose 5% accuracy in engineering applications as a tolerance criterion in the DEM calibration process.

**Table 8.** NSGA-II algorithm setup.

Option	Value
Population Size	500
Number of Generations	200
Crossover Probability	0.9
Crossover Distribution Index	10.0
Mutation Distribution Index	20.0

Table 9 shows the comparison between the DEM simulations and the results of the calibration parameters based on the above optimization. It can be seen from the table that the relative errors of the optimized objective function values are all less than 5%, which indicates that the optimization results are appropriate.

**Table 9.** Error analysis of the optimization results of the objective function.

	$\alpha_{AoR_S}(\circ)$	$\beta_{AoR_D}(\circ)$
Optimization results	32.534	49.058
DEM simulation results	34.094	48.838
Relative error	4.795%	0.448%

#### 4.3. Verification Instance Based on Static Stacking Angle

To verify the correctness of the above calibration procedure, this section verifies the stacking angle of gravel particles via a hollow cylinder lifting test during quasi-static conditions. The validation setup is shown in Figure 14, where non-sticky granular materials are transferred into a hollow Plexiglas cylinder with a diameter of 200 mm and a height of 500 mm, and left to stand to allow the particles to be deposited and stabilized. The surface is to be smoothed, and then the hollow cylinder is lifted at a uniform speed of 0.01 m/s [41]. The particles all flowed freely from the cylinder until the material stabilized in a cone-shaped pile. Then, images are recorded from both directions using a camera, and the images are processed to determine the final stacking angle formed by the stack. The simulation settings were kept consistent with the experimental conditions, and the parameters determined by calibration were used as parameter inputs. The final results are shown in Figure 14.

Table 10 compares the simulated values and experimental measurements after parameter calibration. From the table, it can be seen that the calibrated particle microscopic parameters show better agreement in the hollow cylinder verification test. This verification result is in accordance with the angle of repose tolerance range proposed in this paper.

**Table 10.** Comparison of experimental and simulation results of static stacking angle.

Experiment Serial Number	$\theta_1(\circ)$	$\theta_2(\circ)$	$\theta_3(\circ)$	$\theta_4(\circ)$	$\gamma_s(\circ)$	$\gamma_{s\_mean}(\circ)$
1	30.92	31.88	32.45	29.28	31.13	
2	32.36	32.15	31.50	33.18	32.29	
3	34.51	36.60	34.05	33.62	34.70	32.53
4	34.71	30.46	33.39	33.13	32.92	
5	30.85	31.35	32.15	32.10	31.61	
Optimized Simulation	32.19	31.73	32.05	29.91	31.47	31.47
Relative Error				3.26%		

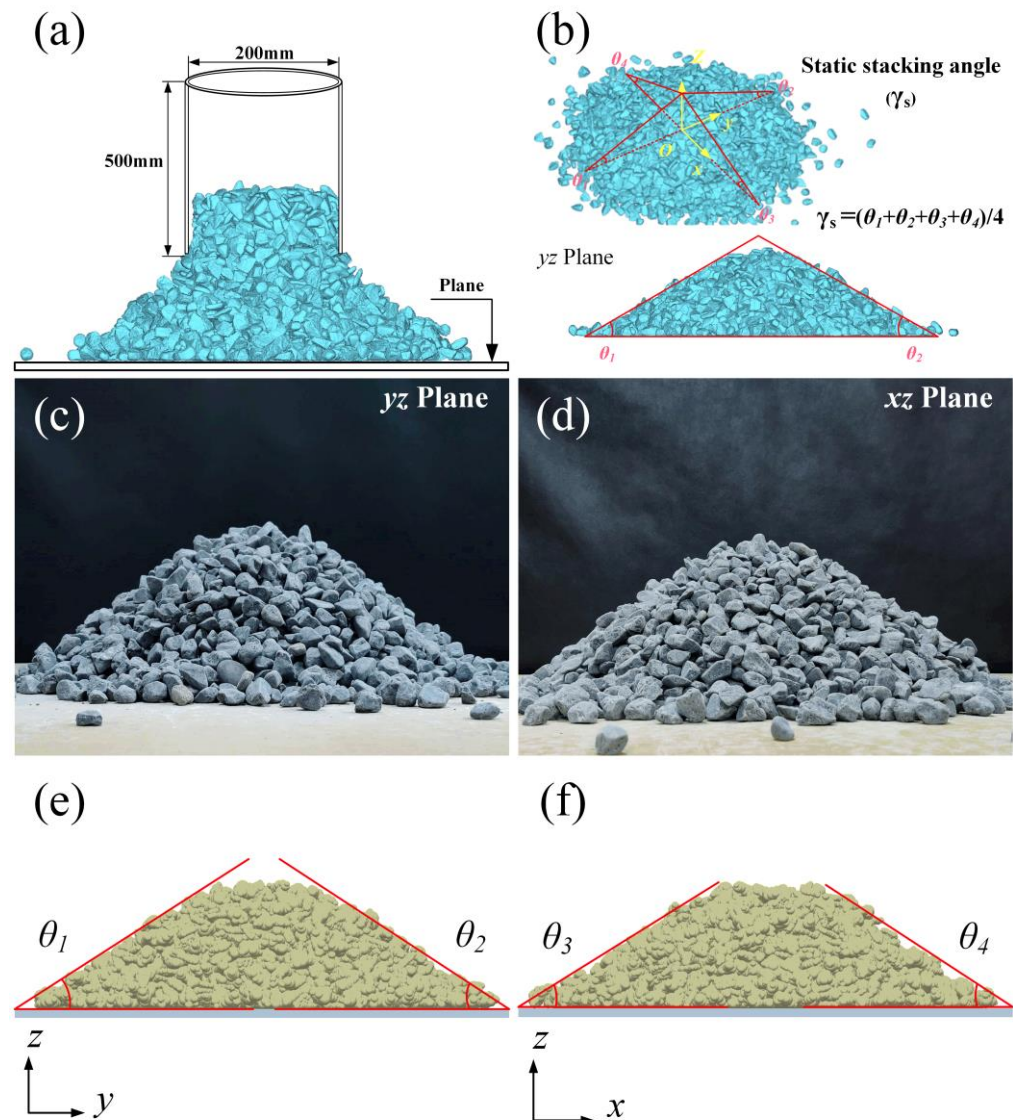


**Figure 14.** The principle of static stacking angle and comparison of results: (a,b) size and measurement settings of test setup; (c,d) results of yz and xz plane test; (e,f) results of yz and xz plane simulation.

#### 4.4. DEM Virtual Test of Solid–Liquid Two-Phase Flow and Wear of Centrifugal Pump

To further illustrate the effectiveness of the application of the calibration parameter set, this section simulates a centrifugal pump at rated operating conditions using coupled CFD–DEM based on the particle model and calibration parameters constructed above. The purpose of the centrifugal pump simulation test is to better understand the development of solid–liquid two-phase flow inside the pump and the occurrence of the primary wear behavior of the pump body. The inlet boundary condition of the centrifugal pump was set to 2.1 m/s, and the outlet was set to free outflow. The RNG  $k$ - $\epsilon$  turbulence model and the slip mesh model were chosen to solve the actual motion of the impeller accurately. The time step of the CFD simulation was set to  $1.15 \times 10^{-5}$  s, during which the impeller rotated approximately  $1^\circ$ . In contrast, the time step of the DEM simulation was set to  $1.15 \times 10^{-6}$  s, with a time step ratio of 1:10 and a synchronous time-saving step of 0.01 s. The total time step is 3600, and the total simulation time is set to 15 T (T represents the time required for one impeller revolution, i.e., 0.04 s/revolution) to ensure the full development of the solid and liquid phases inside the centrifugal pump.

#### 4.4.1. Particle Trajectory Distribution inside the Pump

Figure 15 shows the distribution trajectory of solid particles inside the centrifugal pump with a rated speed of 1450 rpm, a flow rate of  $25 \text{ m}^3/\text{h}$ , and a particle volume fraction of 1% at different moments. To better show the connection between particle velocity and distribution position, particle size is displayed with particle velocity as a scalar in the current view. It can be seen from the figure that the number of particles inside the pump increases from  $t = 0 \text{ s}$  until it stabilizes at  $t = 0.30 \text{ s}$ , when the centrifugal pump reaches a stable operating state. The particles are distributed more uniformly in the inlet section of the pump (Figure 15 (0.05 s)), and when the particles enter the impeller, they enter along the pressure side of the blades (Figure 15; 0.10–0.13 s). As the centrifugal rotation of the impeller accelerates, the particles begin to separate from the impeller. Most of the particles will maintain a stable spiral trajectory during the process from the impeller outlet to the entry into the volute, which is associated with the impeller blade shape (Figure 15; 0.15 s); at this time, most of the particle trajectories are close to the pressure side of the impeller's blade, a trend also shown in the study by Huang et al. [42]. The particles are influenced by their gravity and other comprehensive effects inside the volute. The particles will gather on the wall side of the volute, and the number of particles increases gradually from the tongue side to the outer wall of the volute. Furthermore, some particles hit the outer wall, rebound into the inner wall of the volute flow channel, and stay on the inner wall at a lower speed, as shown in Figure 15 (0.20–0.30 s).

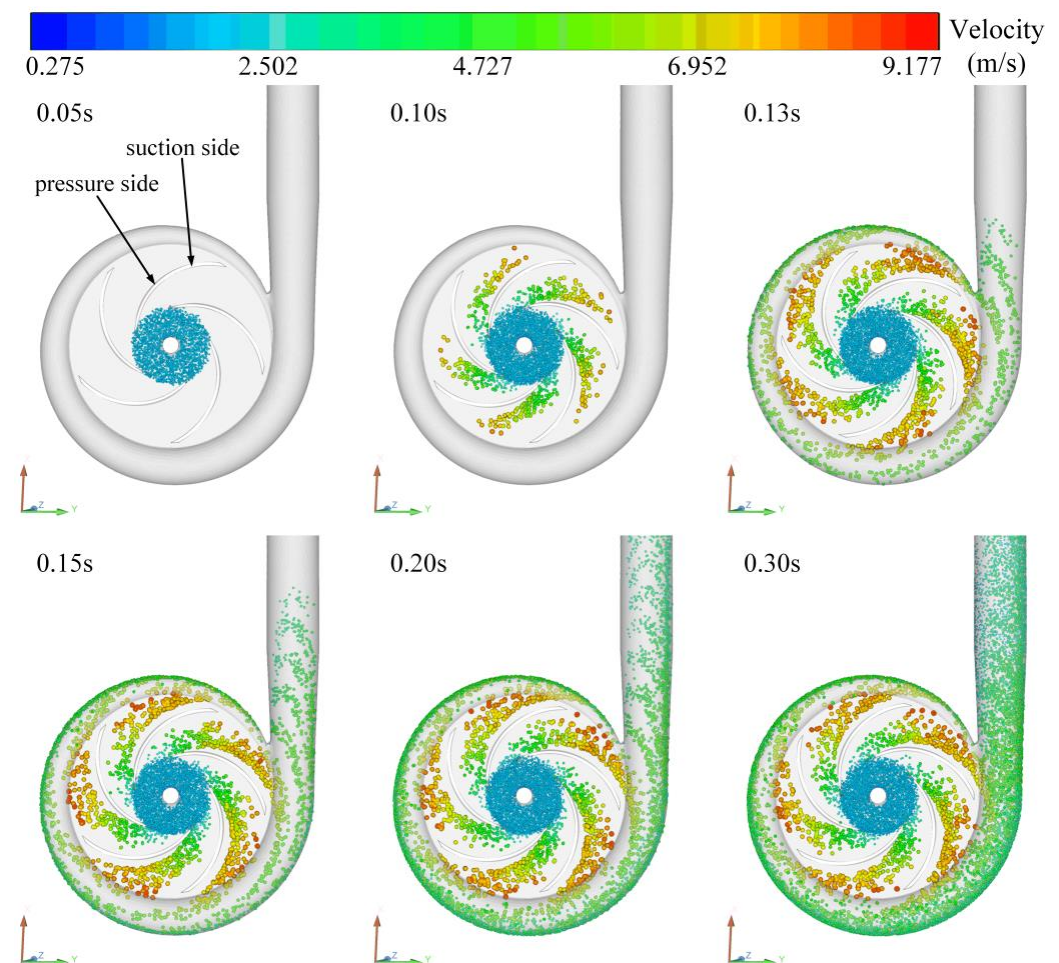
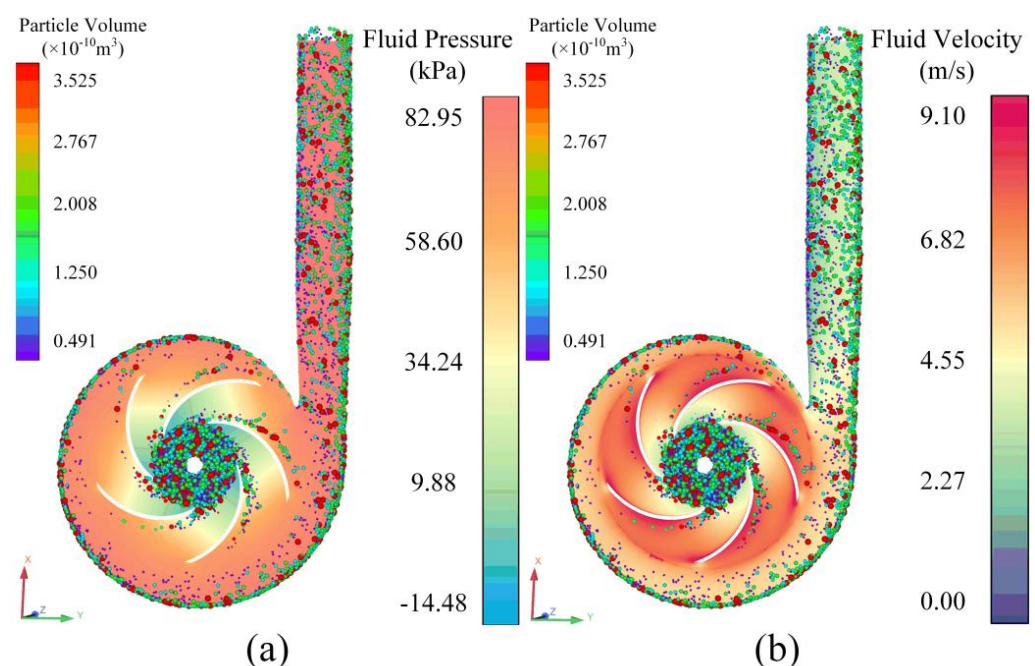


Figure 15. Trajectories of the particles inside the pump at different moments.

#### 4.4.2. Study of Solid–Liquid Two-Phase Characteristics of Centrifugal Pump

Figure 16 shows the solid–liquid two-phase distribution characteristics of the centrifugal pump. From Figure 16a, it can be seen that the most prominent area of pressure change in the pump appears in the impeller region, and mainly shows a gradual increase in pressure from the inlet to the outlet area of the impeller, which is primarily related to the centrifugal effect of the impeller rotation. At the same time, a low-pressure area is generated at the inlet of the centrifugal pump, which is conducive to the solid–liquid mixture that can better enter the interior of the centrifugal pump for transport. It can also be seen that the pressure distribution in the volute is also related to the trend in the solid particle distribution. Figure 16b shows the particle–fluid velocity distribution. The figure shows that in the impeller radial direction, the fluid velocity near the pressure side gradually increases, and near the suction side it gradually decreases. In addition, it can be seen that the particle size distribution is also related to the fluid velocity distribution: the smaller particles are mainly concentrated on the suction side of the impeller and near the inner wall of the volute channel; in comparison, the larger particles are primarily focused on the pressure side of the impeller and the outer wall of the volute. The main reason for this distribution characteristic is that the density of solid particles is larger than the density of the fluid phase; with inertial and centrifugal forces, large particles obtain a higher velocity, showing the phenomenon of clinging to the surface. At the volute outlet, with the increase in the flow channel area and the effect of gravity, the fluid velocity appears to be significantly reduced.



**Figure 16.** Solid–liquid two-phase characteristics of the centrifugal pump ( $t = 0.62$  s): (a) particle–fluid pressure; (b) particle–fluid velocity.

#### 4.4.3. Development of Wear Behavior of Primary Pump Components

In order to study the primary wear behavior of the flow components of centrifugal pumps, this section analyzes the wear behavior of the shroud, blade, hub, and volute of centrifugal pumps with the relative wear model. The model can show the component's wear through normal cumulative contact energy and tangential cumulative contact energy, and reveal the wear mechanism of the element quantitatively through normal contact force and tangential cumulative contact force.

Figure 17a,b shows the distribution of the normal/tangential cumulative contact energy of the impeller, from which it can be seen that the pressure side of the impeller

and the hub are most likely to experience wear behavior, and the closer the area to the impeller axis the further the wear appears. The head of the blade is the point at which the maximum value of normal cumulative energy is reached, which indicates that this part is more likely to experience wear behavior. The main reason for this phenomenon is related to the erosive wear in the area where the particles enter the impeller from the inlet. In addition, the interaction between the impeller and the particles, on the one hand, increases the particle velocity; on the other hand, the particles have a cutting effect on the blade's pressure surface, further aggravating the appearance of wear behavior.

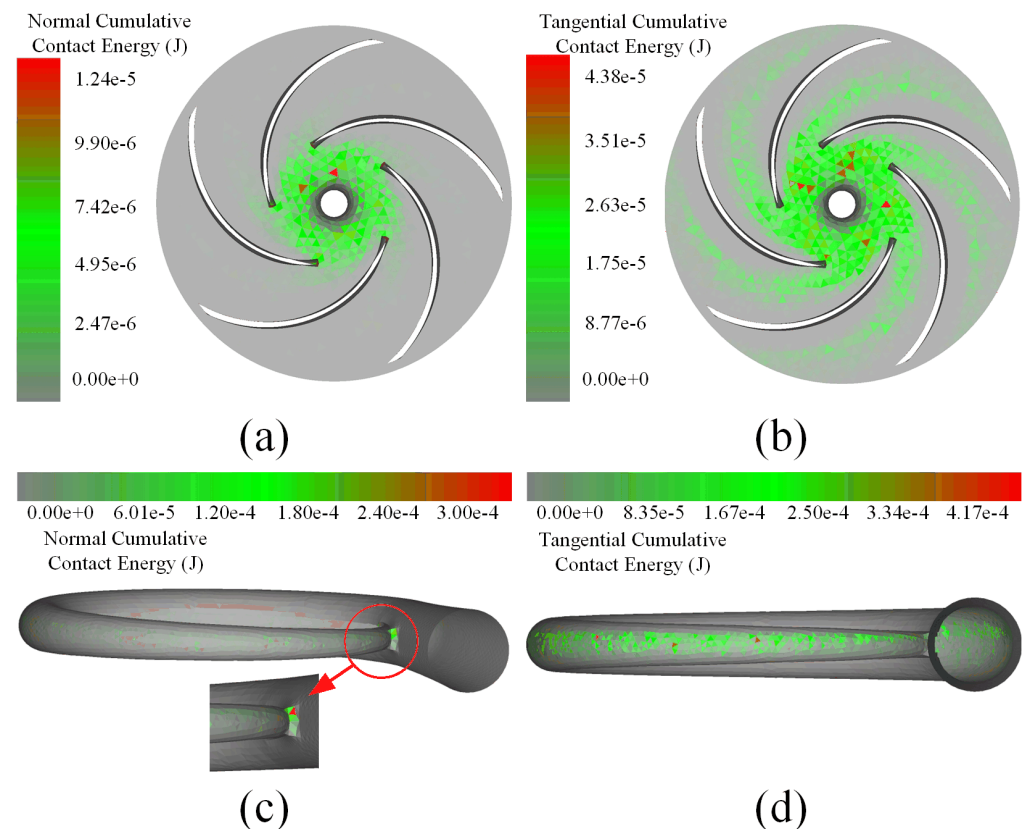


**Figure 17.** Schematic distribution of contact energy between impeller and volute: (a,c) normal cumulative contact energy; (b,d) tangential cumulative contact energy.

Figure 17c,d shows the cumulative contact energy of the volute. The tongue and volute are the primary areas where wear occurs, which is strongly related to the trajectory of the particles. After gaining a large velocity through the impeller, the particles move with the fluid phase in the volute channel. The tangential velocity of the particles interacts with the volute wall surface, deepening the volute wall's wear. In addition, the wear range occurring on the volute wall also closely correlates with the accumulation location in particle movement.

To further reveal the wear mechanism of the components of the centrifugal pump, stress analysis of the main components in the pump is performed in this section. The results of the average accumulated contact force variation for each part are shown in Figure 18. In the  $t = 0$  s to  $t = 0.1$  s stage, the accumulated contact force of the components is 0, which is mainly because the length of the inlet extension prevents the particle group from moving to the internal centrifugal pump. There is no contact with the components. After  $t = 0.1$  s, the particles begin to contact the flow parts, which causes wear. Each component's average cumulative contact force change is linearly related to time. It can be seen that the average cumulative contact force of the volute is larger than the rest of the components. As demonstrated in Figure 17, the volute is the component where the most severe wear behavior occurs. The wear behavior of the volute mainly originates from the increase in

the accumulated tangential force of the particles on the volute. After accelerating through the impeller to obtain a more significant velocity, most of the particles cause tangential action on the spiral surface of the volute. In addition, it can also be seen from the figure that the average cumulative contact force of the blade and hub also changes more significantly. In the  $t = 0$  s to  $t = 0.3$  s stage, the blade's normal contact force is higher than the rest of the components, which is directly related to the trajectory of the particles in Section 4.4.1: At this time, the particles enter the impeller area from the inlet section, and a direct collision with the blade head occurs to form impact behavior. As the number of particles entering the system, and their motion, stabilizes, more particles interact with the large contact area of the volute, eventually causing the cumulative contact force of the volute to increase rapidly.

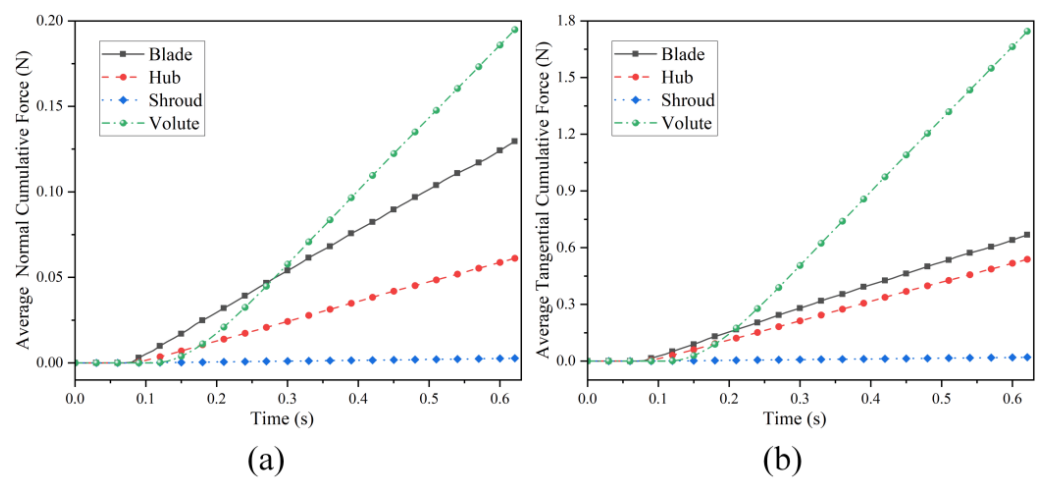


**Figure 18.** Variation in the average cumulative contact force for different components: (a) normal cumulative contact force; (b) tangential cumulative contact force.

## 5. Conclusions

This paper uses simulation tests and optimization algorithms to calibrate and verify the angle of repose of gravel materials in centrifugal slurry pump conditions. Considering the problems of parameter combination ambiguity and particle model accuracy, this paper proposes a multi-objective optimization method with the static and dynamic angle of repose as the response values of irregular gravel materials. Further experimental validation shows that the procedure can be accurately applied to the calibration of flow parameters of irregular bulk materials. The main conclusions are as follows:

- (1) This paper constructs a more accurate particle irregular multi-sphere model based on the original gravel 3D scanning model. It combines the independent angle of repose test and the image analysis method to measure gravel's angle of repose. The well-estimated results of the angle of repose show that the scheme is an accurate and efficient method for obtaining the angle of repose values for irregular materials. The results of the sensitivity study of the DEM parameters show that the intrinsic parameters of the particles in the simulation (Poisson's ratio, Young's modulus, and particle density) and the collision recovery coefficient do not have a significant effect on the angle of repose. However, a moderate reduction in Young's modulus could significantly reduce the computational cost.
- (2) In this paper, the design variables are obtained by LHS, and the  $R^2$  values of the static and dynamic angle of repose in the multi-objective optimal design model constructed by the RBF model as a surrogate model are 0.965 and 0.958, respectively. This result indicates that the established surrogate model can accurately reflect the relationship between particle micro-parameters and macro-responses. The parameter sensitivity analysis of the optimized model showed that the sliding friction coefficient had the most significant influence on the macroscopic angle of repose of the particles.

The best combinations of gravel particle simulation parameters were also obtained, i.e., the particle–particle sliding friction coefficient of 0.323, the particle–particle rolling friction coefficient of 0.061, the particle–geometric sliding friction coefficient of 0.316, and particle–geometric rolling friction coefficient of 0.441.

- (3) The results of the validation test of gravel stacking angle with the optimal combination of parameters show that the relative error between the DEM simulated value and the physical test stacking angle is 3.26%, which is within the allowable tolerance of the angle of repose. The particle stacking shape of the simulated test almost remains consistent with the physical test. The above results show that the new optimization model constructed in this study can be realistically and reliably applied to the calibration of flow parameters of gravel particles.
- (4) The CFD–DEM coupling method was used to analyze the solid–liquid two-phase transient flow inside the centrifugal pump. The results show that the particle trajectory distribution inside the centrifugal pump exhibits a direct connection with the centrifugal force and gravity on the particles and the shape of the impeller. The volute is the most severely impacted component of the centrifugal pump in terms of wear. The increase in the cumulative tangential contact force of the volute is the essential factor in generating the wear behavior. This study only analyzes the development of solid–liquid flow and wear behavior inside centrifugal pumps and verifies the validity of the calibrated parameter set for application in industrial scenarios. The interaction mechanisms between the particles and the components inside the pump and the related applications will be further investigated in detail in the future.

**Author Contributions:** Conceptualization, A.Z.; Methodology, A.Z.; Software, A.Z., Y.F. and H.W.; Validation, Y.F., Z.W. and Q.G.; Investigation, Y.F., Q.G. and H.W.; Resources, Z.W.; Writing—Original Draft Preparation, A.Z.; Writing—Review and Editing, A.Z.; Supervision, Z.W. and Q.G.; Project Administration, Z.W.; Funding Acquisition, Z.W. All authors have read and agreed to the published version of the manuscript.

**Funding:** This research was funded by the National Natural Science Foundation of China (51875419) and the Key Research and Development Projects in Hubei Province (2020BAB138).

**Institutional Review Board Statement:** Not applicable.

**Informed Consent Statement:** Not applicable.

**Data Availability Statement:** Data are contained within the article. All the code generated or used during the study are available from the corresponding author.

**Conflicts of Interest:** The authors declare no conflict of interest.

## Appendix A

Design Variables				Actual Value		Predicted Value	
$\mu_{s\_pp}$	$\mu_{r\_pp}$	$\mu_{s\_pw}$	$\mu_{r\_pw}$	$\alpha_{AoR\_S}/^\circ$	$\beta_{AoR\_D}/^\circ$	$\alpha_{AoR\_S}/^\circ$	$\beta_{AoR\_D}/^\circ$
0.519	0.343	0.761	0.248	40.3	62.9	-	-
0.289	0.080	0.070	0.678	17.8	17.4	-	-
0.258	0.008	0.144	0.650	25.0	28.8	-	-
0.579	0.040	0.158	0.657	32.3	33.9	-	-
0.529	0.160	0.181	0.782	34.8	37.1	-	-
0.584	0.105	0.060	0.779	22.0	17.8	-	-
0.177	0.329	0.533	0.427	28.3	54.1	-	-
0.208	0.222	0.234	0.331	27.6	41.0	-	-
0.141	0.434	0.292	0.079	23.7	44.3	-	-
0.623	0.191	0.178	0.604	37.9	34.6	-	-
0.002	0.144	0.080	0.715	7.9	17.2	-	-
0.794	0.099	0.054	0.791	26.7	16.5	-	-

---

0.277	0.059	0.189	0.617	28.2	34.1	-	-
0.729	0.156	0.022	0.672	7.4	14.6	-	-
0.451	0.021	0.006	0.613	2.0	11.0	-	-
0.160	0.559	0.376	0.576	23.9	49.4	-	-
0.153	0.180	0.193	0.755	22.2	35.3	-	-
0.604	0.686	0.099	0.646	29.0	30.3	-	-
0.214	0.762	0.131	0.625	20.1	27.3	-	-
0.709	0.732	0.064	0.631	19.6	25.9	-	-
0.191	0.627	0.040	0.774	5.8	11.7	-	-
0.098	0.663	0.001	0.642	1.2	5.2	-	-
0.102	0.638	0.013	0.731	4.9	6.7	-	-
0.649	0.700	0.122	0.661	31.9	31.1	-	-
0.678	0.744	0.026	0.762	7.9	17.5	-	-
0.031	0.658	0.126	0.684	8.1	22.1	-	-
0.287	0.239	0.662	0.293	34.6	56.9	-	-
0.317	0.475	0.779	0.117	35.1	62.7	-	-
0.273	0.595	0.372	0.307	30.2	54.5	-	-
0.114	0.339	0.559	0.189	24.1	53.9	-	-
0.585	0.582	0.469	0.273	37.1	66.6	-	-
0.000	0.438	0.706	0.529	12.5	40.9	-	-
0.257	0.598	0.481	0.539	30.7	57.5	-	-
0.666	0.348	0.552	0.032	42.8	66.3	-	-
0.098	0.510	0.227	0.122	17.1	29.9	-	-
0.565	0.524	0.737	0.212	41.1	68.1	-	-
0.371	0.575	0.635	0.283	35.3	60.7	-	-
0.599	0.441	0.796	0.342	40.6	66.8	-	-
0.399	0.534	0.537	0.156	34.6	58.4	-	-
0.498	0.378	0.443	0.235	38.7	58.1	-	-
0.232	0.527	0.494	0.255	29.2	53.9	-	-
0.054	0.322	0.334	0.084	17.6	40.2	-	-
0.655	0.591	0.583	0.420	39.1	70.5	-	-
0.761	0.360	0.418	0.329	42.6	62.2	-	-
0.018	0.551	0.510	0.337	13.8	40.0	-	-
0.453	0.463	0.592	0.225	37.4	66.9	-	-
0.336	0.346	0.322	0.295	33.6	52.0	-	-
0.409	0.210	0.317	0.434	35.5	52.3	-	-
0.692	0.516	0.546	0.321	39.4	66.4	-	-
0.490	0.301	0.646	0.516	40.2	63.9	-	-
0.218	0.312	0.525	0.410	29.6	55.2	-	-
0.359	0.392	0.486	0.016	36.2	57.3	-	-
0.508	0.381	0.327	0.132	37.8	55.7	-	-
0.404	0.586	0.250	0.495	32.4	45.0	-	-
0.243	0.494	0.416	0.095	29.5	52.6	-	-
0.746	0.327	0.784	0.269	44.4	62.4	-	-
0.555	0.371	0.748	0.573	39.6	62.9	-	-
0.154	0.266	0.774	0.023	27.2	52.3	-	-
0.083	0.466	0.440	0.101	19.4	41.7	-	-
0.447	0.246	0.401	0.352	39.2	51.3	-	-
0.436	0.218	0.741	0.141	41.8	61.4	-	-
0.768	0.305	0.210	0.452	38.7	43.7	-	-
0.781	0.414	0.273	0.393	37.9	57.8	-	-
0.347	0.387	0.263	0.069	30.4	46.5	-	-
0.367	0.200	0.388	0.259	35.9	55.2	-	-
0.030	0.444	0.206	0.543	11.4	28.2	-	-
0.130	0.520	0.457	0.491	23.5	50.7	-	-
0.646	0.552	0.694	0.003	41.2	66.3	-	-
0.546	0.577	0.259	0.217	34.1	44.3	-	-
0.297	0.532	0.246	0.448	27.5	41.3	-	-

---

0.040	0.319	0.268	0.521	14.6	38.4	-	-
0.332	0.483	0.643	0.363	35.8	58.5	-	-
0.703	0.253	0.424	0.038	44.2	58.5	-	-
0.631	0.315	0.769	0.441	44.7	62.8	-	-
0.150	0.296	0.304	0.025	23.5	40.7	-	-
0.614	0.241	0.512	0.173	43.2	61.3	-	-
0.678	0.421	0.381	0.078	42.1	61.8	-	-
0.065	0.454	0.523	0.467	18.4	45.1	-	-
0.622	0.205	0.282	0.461	40.6	56.4	-	-
0.077	0.404	0.431	0.200	19.8	45.3	-	-
0.190	0.232	0.718	0.525	29.8	57.1	-	-
0.734	0.547	0.473	0.198	39.1	64.9	-	-
0.484	0.259	0.340	0.356	37.9	54.5	-	-
0.013	0.296	0.658	0.104	14.9	40.9	-	-
0.793	0.229	0.586	0.384	45.8	64.7	-	-
0.235	0.570	0.352	0.505	28.8	47.3	-	-
0.196	0.226	0.728	0.468	29.8	54.2	-	-
0.785	0.536	0.625	0.588	45.1	66.0	-	-
0.582	0.270	0.598	0.559	42.7	62.8	-	-
0.122	0.290	0.565	0.109	24.0	52.2	-	-
0.205	0.565	0.652	0.011	30.0	54.7	-	-
0.088	0.274	0.758	0.504	21.8	47.4	-	-
0.291	0.450	0.407	0.556	32.5	55.2	-	-
0.424	0.367	0.214	0.282	33.0	42.0	-	-
0.106	0.364	0.576	0.388	22.7	49.8	-	-
0.721	0.250	0.358	0.166	43.5	59.1	-	-
0.535	0.471	0.240	0.184	33.6	48.8	-	-
0.427	0.540	0.627	0.597	37.7	64.4	-	-
0.540	0.397	0.363	0.062	38.8	65.3	-	-
0.176	0.334	0.678	0.318	28.5	51.4	-	-
0.053	0.112	0.136	0.670	13.7	23.1	15.0	25.7
0.508	0.019	0.089	0.711	30.1	20.2	25.7	24.1
0.129	0.131	0.118	0.705	18.8	24.2	16.4	23.4
0.545	0.127	0.170	0.728	35.6	39.4	35.0	34.3
0.305	0.175	0.080	0.797	20.8	20.9	22.7	21.2
0.392	0.070	0.092	0.749	31.2	23.6	28.0	21.0
0.161	0.062	0.105	0.698	18.3	22.5	19.7	22.2
0.780	0.032	0.147	0.693	33.4	33.3	37.6	27.9
0.497	0.676	0.112	0.725	26.7	28.4	24.6	27.6
0.697	0.778	0.197	0.770	31.3	43.0	36.0	32.6
0.468	0.715	0.019	0.754	4.4	17.9	7.2	17.2
0.375	0.616	0.038	0.708	7.4	15.8	10.7	22.4
0.347	0.694	0.047	0.687	9.4	21.2	8.8	16.0
0.426	0.753	0.151	0.744	25.9	31.7	26.4	33.5
0.472	0.502	0.792	0.375	38.1	65.5	38.3	65.1
0.065	0.792	0.165	0.606	11.1	29.3	11.1	27.6
0.415	0.783	0.168	0.738	26.9	34.9	26.5	33.1
0.337	0.609	0.073	0.786	14.6	26.2	9.3	16.4
0.743	0.725	0.033	0.635	10.4	22.6	12.7	21.4
0.220	0.647	0.107	0.623	18.3	21.8	15.8	21.2
0.380	0.431	0.447	0.585	34.3	56.6	36.8	59.6
0.522	0.277	0.700	0.367	41.0	61.2	41.8	62.4
0.035	0.283	0.615	0.398	17.5	42.9	18.8	45.2
0.608	0.424	0.299	0.056	37.5	57.0	38.3	58.9
0.681	0.459	0.462	0.230	40.2	64.2	40.4	65.3
0.387	0.488	0.223	0.155	31.4	42.3	30.0	41.2
0.272	0.401	0.608	0.477	33.3	59.8	32.4	58.0

0.576	0.486	0.716	0.047	39.1	67.3	41.1	66.6
0.469	0.287	0.571	0.146	39.8	57.6	40.4	62.2
0.758	0.260	0.681	0.305	45.8	65.5	45.3	63.4
0.635	0.498	0.287	0.180	37.3	58.9	36.5	53.7
0.743	0.355	0.395	0.548	44.2	66.8	42.5	60.9
0.308	0.504	0.347	0.205	32.0	42.9	31.6	51.4
0.057	0.412	0.492	0.480	18.2	43.1	18.3	45.2
0.657	0.417	0.505	0.569	40.3	69.3	43.2	66.6
0.707	0.373	0.605	0.420	42.4	66.9	43.0	66.9
0.716	0.214	0.314	0.132	44.4	53.5	41.5	55.4
0.322	0.477	0.727	0.405	34.9	59.9	35.4	58.4
0.463	0.563	0.671	0.245	36.7	65.8	38.1	66.7
0.252	0.388	0.687	0.048	32.7	59.6	32.9	58.7

## References

- Perissinotto, R.M.; Monte Verde, W.; de Castro, M.S.; Biazussi, J.L.; Estevam, V.; Bannwart, A.C. Experimental Investigation of Oil Drops Behavior in Dispersed Oil-Water Two-Phase Flow within a Centrifugal Pump Impeller. *Exp. Therm. Fluid Sci.* **2019**, *105*, 11–26. [\[CrossRef\]](#)
- Chen, R.; Deng, S.; Zhao, L.; Zhao, R.; Xu, W. Energy Recovery from Wastewater in Deep-Sea Mining: Feasibility Study on an Energy Supply Solution with Cold Wastewater. *Appl. Energy* **2022**, *305*, 117719. [\[CrossRef\]](#)
- Wang, R.; Zhu, Z.; Su, X.; Mianowicz, K.; Jia, H.; Wu, K. Slurry Pumps in Deep-Sea Mining: A Review of Numerical and Experimental Studies. *Ocean Eng.* **2022**, *251*, 111150. [\[CrossRef\]](#)
- Shihab, T.A.; Shlapak, L.S.; Namer, N.S.; Pryszyazhnyuk, P.M.; Ivanov, O.O.; Burda, M.J. Increasing of Durability of Mechanical Seals of Oil and Gas Centrifugal Pumps Using Tungsten-Free Cermet with Cu-Ni-Mn Binder. *J. Phys. Conf. Ser.* **2021**, *1741*, 012031. [\[CrossRef\]](#)
- Ramirez, R.; Avila, E.; Lopez, L.; Bula, A.; Duarte Forero, J. CFD Characterization and Optimization of the Cavitation Phenomenon in Dredging Centrifugal Pumps. *Alex. Eng. J.* **2020**, *59*, 291–309. [\[CrossRef\]](#)
- Roco, M.C.; Addie, G.R.; Visintainer, R. Study on Casing Performances in Centrifugal Slurry Pumps. *Part. Sci. Technol.* **1985**, *3*, 65–88. [\[CrossRef\]](#)
- Tarodiya, R.; Gandhi, B.K. Numerical Simulation of a Centrifugal Slurry Pump Handling Solid-Liquid Mixture: Effect of Solids on Flow Field and Performance. *Adv. Powder Technol.* **2019**, *30*, 2225–2239. [\[CrossRef\]](#)
- Ma, C.; Yang, J.; Zenz, G.; Staudacher, E.J.; Cheng, L. Calibration of the Microparameters of the Discrete Element Method Using a Relevance Vector Machine and Its Application to Rockfill Materials. *Adv. Eng. Softw.* **2020**, *147*, 102833. [\[CrossRef\]](#)
- Benvenuti, L.; Kloss, C.; Pirker, S. Identification of DEM Simulation Parameters by Artificial Neural Networks and Bulk Experiments. *Powder Technol.* **2016**, *291*, 456–465. [\[CrossRef\]](#)
- Hesse, R.; Krull, F.; Antonyuk, S. Prediction of Random Packing Density and Flowability for Non-Spherical Particles by Deep Convolutional Neural Networks and Discrete Element Method Simulations. *Powder Technol.* **2021**, *393*, 559–581. [\[CrossRef\]](#)
- Wang, M.; Lu, Z.; Wan, W.; Zhao, Y. A Calibration Framework for the Microparameters of the DEM Model Using the Improved PSO Algorithm. *Adv. Powder Technol.* **2021**, *32*, 358–369. [\[CrossRef\]](#)
- Schiochet Nasato, D.; Queiroz Albuquerque, R.; Briesen, H. Predicting the Behavior of Granules of Complex Shapes Using Coarse-Grained Particles and Artificial Neural Networks. *Powder Technol.* **2021**, *383*, 328–335. [\[CrossRef\]](#)
- He, P.; Fan, Y.; Pan, B.; Zhu, Y.; Liu, J.; Zhu, D. Calibration and Verification of Dynamic Particle Flow Parameters by the Back-Propagation Neural Network Based on the Genetic Algorithm: Recycled Polyurethane Powder. *Materials* **2019**, *12*, 3350. [\[CrossRef\]](#)
- Degrassi, G.; Parussini, L.; Boscolo, M.; Petronelli, N.; Dimastromatteo, V. Discrete Element Simulation of the Charge in the Hopper of a Blast Furnace, Calibrating the Parameters through an Optimization Algorithm. *SN Appl. Sci.* **2021**, *3*, 242. [\[CrossRef\]](#)
- Richter, C.; Röfler, T.; Kunze, G.; Katterfeld, A.; Will, F. Development of a Standard Calibration Procedure for the DEM Parameters of Cohesionless Bulk Materials—Part II: Efficient Optimization-Based Calibration. *Powder Technol.* **2020**, *360*, 967–976. [\[CrossRef\]](#)
- Qu, T.; Feng, Y.T.; Zhao, T.; Wang, M. Calibration of Linear Contact Stiffnesses in Discrete Element Models Using a Hybrid Analytical-Computational Framework. *Powder Technol.* **2019**, *356*, 795–807. [\[CrossRef\]](#)
- Qu, T.; Feng, Y.; Zhao, T.; Wang, M. A Hybrid Calibration Approach to Hertz-type Contact Parameters for Discrete Element Models. *Int. J. Numer. Anal. Methods Geomech.* **2020**, *44*, 1281–1300. [\[CrossRef\]](#)
- Qu, T.; Feng, Y.T.; Zhao, J. A Strain Energy-Based Elastic Parameter Calibration Method for Lattice/Bonded Particle Modelling of Solid Materials. *Powder Technol.* **2022**, *410*, 117860. [\[CrossRef\]](#)
- Coetzee, C.J. Calibration of the Discrete Element Method and the Effect of Particle Shape. *Powder Technol.* **2016**, *297*, 50–70. [\[CrossRef\]](#)
- Cabiscol, R.; Finke, J.H.; Kwade, A. Calibration and Interpretation of DEM Parameters for Simulations of Cylindrical Tablets with Multi-Sphere Approach. *Powder Technol.* **2018**, *327*, 232–245. [\[CrossRef\]](#)

21. Luo, X.; Zhao, L.; Dong, H. Study on DEM Parameter Calibration and Wear Characteristics of Vanadium-Titanium Magnetite Pellets. *Powder Technol.* **2021**, *393*, 427–440. [[CrossRef](#)]
22. Barrios, G.K.P.; de Carvalho, R.M.; Kwade, A.; Tavares, L.M. Contact Parameter Estimation for DEM Simulation of Iron Ore Pellet Handling. *Powder Technol.* **2013**, *248*, 84–93. [[CrossRef](#)]
23. Li, T.; Peng, Y.; Zhu, Z.; Zou, S.; Yin, Z. Discrete Element Method Simulations of the Inter-Particle Contact Parameters for the Mono-Sized Iron Ore Particles. *Materials* **2017**, *10*, 520. [[CrossRef](#)]
24. Xu, L.; Luo, K.; Zhao, Y.; Fan, J.; Cen, K. Influence of Particle Shape on Liner Wear in Tumbling Mills: A DEM Study. *Powder Technol.* **2019**, *350*, 26–35. [[CrossRef](#)]
25. Tang, C.; Yang, Y.-C.; Liu, P.-Z.; Kim, Y.-J. Prediction of Abrasive and Impact Wear Due to Multi-Shaped Particles in a Centrifugal Pump via CFD-DEM Coupling Method. *Energies* **2021**, *14*, 2391. [[CrossRef](#)]
26. Arntz, M.M.H.D.; den Otter, W.K.; Briels, W.J.; Bussmann, P.J.T.; Beeftink, H.H.; Boom, R.M. Granular Mixing and Segregation in a Horizontal Rotating Drum: A Simulation Study on the Impact of Rotational Speed and Fill Level. *AIChE J.* **2008**, *54*, 3133–3146. [[CrossRef](#)]
27. Mehta, A.; Barker, G.C. The Dynamics of Sand. *Rep. Prog. Phys.* **1994**, *57*, 383. [[CrossRef](#)]
28. Tripathi, A.; Kumar, V.; Agarwal, A.; Tripathi, A.; Basu, S.; Chakrabarty, A.; Nag, S. Quantitative DEM Simulation of Pellet and Sinter Particles Using Rolling Friction Estimated from Image Analysis. *Powder Technol.* **2021**, *380*, 288–302. [[CrossRef](#)]
29. Jiang, S.; Ye, Y.; He, M.; Duan, C.; Liu, S.; Liu, J.; Xiao, X.; Zhang, H.; Tan, Y. Mixing Uniformity of Irregular Sand and Gravel Materials in a Rotating Drum with Determination of Contact Model Parameters. *Powder Technol.* **2019**, *354*, 377–391. [[CrossRef](#)]
30. Qu, T.; Feng, Y.; Wang, M. An Adaptive Granular Representative Volume Element Model with an Evolutionary Periodic Boundary for Hierarchical Multiscale Analysis. *Int. J. Numer. Methods Eng.* **2021**, *122*, 2239–2253. [[CrossRef](#)]
31. Wadell, H. Volume, Shape, and Roundness of Quartz Particles. *J. Geol.* **1935**, *43*, 250–280. [[CrossRef](#)]
32. Zhou, Y.C.; Xu, B.H.; Yu, A.B.; Zulli, P. An Experimental and Numerical Study of the Angle of Repose of Coarse Spheres. *Powder Technol.* **2002**, *125*, 45–54. [[CrossRef](#)]
33. Yan, Z.; Wilkinson, S.K.; Stitt, E.H.; Marigo, M. Discrete Element Modelling (DEM) Input Parameters: Understanding Their Impact on Model Predictions Using Statistical Analysis. *Comput. Part. Mech.* **2015**, *2*, 283–299. [[CrossRef](#)]
34. Wensrich, C.M.; Katterfeld, A. Rolling Friction as a Technique for Modelling Particle Shape in DEM. *Powder Technol.* **2012**, *217*, 409–417. [[CrossRef](#)]
35. Roessler, T.; Richter, C.; Katterfeld, A.; Will, F. Development of a Standard Calibration Procedure for the DEM Parameters of Cohesionless Bulk Materials—Part I: Solving the Problem of Ambiguous Parameter Combinations. *Powder Technol.* **2019**, *343*, 803–812. [[CrossRef](#)]
36. Hong, H.; Zhang, Z.; Guo, A.; Shen, L.; Sun, H.; Liang, Y.; Wu, F.; Lin, H. Radial Basis Function Artificial Neural Network (RBF ANN) as Well as the Hybrid Method of RBF ANN and Grey Relational Analysis Able to Well Predict Trihalomethanes Levels in Tap Water. *J. Hydrol.* **2020**, *591*, 125574. [[CrossRef](#)]
37. Fan, Y.; Wang, Z.; Fu, T. Multi-Objective Optimization Design of Lithium-Ion Battery Liquid Cooling Plate with Double-Layered Dendritic Channels. *Appl. Therm. Eng.* **2021**, *199*, 117541. [[CrossRef](#)]
38. Deb, K.; Pratap, A.; Agarwal, S.; Meyarivan, T. A Fast and Elitist Multiobjective Genetic Algorithm: NSGA-II. *IEEE Trans. Evol. Comput.* **2002**, *6*, 182–197. [[CrossRef](#)]
39. Qu, T.; Feng, Y.T.; Wang, M.; Jiang, S. Calibration of Parallel Bond Parameters in Bonded Particle Models via Physics-Informed Adaptive Moment Optimisation. *Powder Technol.* **2020**, *366*, 527–536. [[CrossRef](#)]
40. Qu, T.; Feng, Y.T.; Wang, Y.; Wang, M. Discrete Element Modelling of Flexible Membrane Boundaries for Triaxial Tests. *Comput. Geotech.* **2019**, *115*, 103154. [[CrossRef](#)]
41. Aela, P.; Zong, L.; Esmaili, M.; Siahkouhi, M.; Jing, G. Angle of Repose in the Numerical Modeling of Ballast Particles Focusing on Particle-Dependent Specifications: Parametric Study. *Particuology* **2022**, *65*, 39–50. [[CrossRef](#)]
42. Huang, S.; Su, X.; Qiu, G. Transient Numerical Simulation for Solid-Liquid Flow in a Centrifugal Pump by DEM-CFD Coupling. *Eng. Appl. Comput. Fluid Mech.* **2015**, *9*, 411–418. [[CrossRef](#)]

**Disclaimer/Publisher's Note:** The statements, opinions and data contained in all publications are solely those of the individual author(s) and contributor(s) and not of MDPI and/or the editor(s). MDPI and/or the editor(s) disclaim responsibility for any injury to people or property resulting from any ideas, methods, instructions or products referred to in the content.